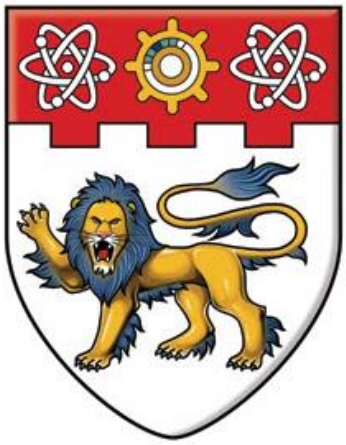

NANYANG TECHNOLOGICAL UNIVERSITY

MODELLING OF GRAIN STRUCTURE USING CELLULAR AUTOMATA-FINITE ELEMENT METHOD FOR ADDITIVE MANUFACTURING OF METALS

TAN HEANG KUAN JOEL
SCHOOL OF MECHANICAL AND AEROSPACE ENGINEERING
2021

MODELLING OF GRAIN STRUCTURE USING CELLULAR AUTOMATA-FINITE ELEMENT METHOD FOR ADDITIVE MANUFACTURING OF METALS

TAN HEANG KUAN JOEL

School of Mechanical and Aerospace Engineering

A thesis submitted to the Nanyang Technological University in partial fulfilment of the requirement for the degree of Masters in Engineering.

2021

Statement of Originality

I hereby certify that the work embodied in this thesis is the result of original research, is free of plagiarised materials, and has not been submitted for a higher degree to any other University or Institution.

18/03/2021

. . . .

Date Tan Heang Kuan Joel

Supervisor Declaration Statement

I have reviewed the content and presentation style of this thesis and declare it is free of plagiarism and of sufficient grammatical clarity to be examined. To the best of my knowledge, the research and writing are those of the candidate except as acknowledged in the Author Attribution Statement. I confirm that the investigations were conducted in accord with the ethics policies and integrity standards of Nanyang Technological University and that the research data are presented honestly and without prejudice.

18/03/2021 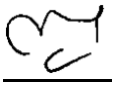

. . . .

Date Assoc Prof Yeong Wai Yee

Authorship Attribution Statement

This thesis contains material from 1 paper(s) published in the following peer-reviewed journal(s) / from papers accepted at conferences in which I am listed as an author.

Chapter 2 is published as J.H.K. Tan, S.L. Sing, W.Y. Yeong.

Microstructure modelling for metallic additive manufacturing: a review. Virtual and Physical Prototyping, 15:1, 87-105 (2020).

DOI: 10.1080/17452759.2019.1677345

The contributions of the co-authors are as follows:

- Assoc Prof Yeong provided guidance on the project direction and edited the manuscript drafts.
- I prepared the manuscript drafts. The manuscript was revised by Dr Sing.

18/03/2021

. . . . . .

Date

. . . . . .

Tan Heang Kuan Joel

Acknowledgements

The author wishes to express his heartfelt gratitude to his supervisor, Associate Professor Yeong Wai Yee for her academic guidance, supervision and patience throughout his candidature. The author also likes to thank Dr Sing Swee Leong and Huang Sheng for providing the author with valuable guidance and critical advices.

The author likes to express his heartfelt gratitude to all laboratory specialists, technicians and managers from the School of Mechanical and Aerospace Engineering, Nanyang Technological University who have provided assistance to the author.

The author thanks his family and friends for their constant support and encouragement.

Table of Contents

Summary x

List of Figures xi

List of Tables xiv

List of Abbreviations xv

Nomenclature xvi

Chapter 1 Introduction 1

1.1 Background 1

1.2 Significance of the Problem and its Challenges 2

1.3 Objectives and Scope 2

1.4 Potential Contributions 4

1.5 Organization of Report 4

Chapter 2 Literature Review 6

2.1 Additive Manufacturing Methods for Metals 6

2.2 Grain Structure of Additively Manufactured Metals 7

2.2.1 Theory of Solidification 8

2.2.2 Experimental Observations of Additively Manufactured Metals 21

2.3 Modelling of Microstructure for Additively Manufactured Metals 23

2.3.1 Thermal Models 24

2.3.2 Microstructure Models 28

2.3.3 Comparison of Modelling Methods 35
2.3.4 Validation and Comparison of Simulation Models Against Experimental Results 36
2.4 Research Gap 37
Chapter 3 Methodology 39
3.1 Finite Element Method 40
3.1.1 Stainless Steel 316L 42
3.1.2 Ti34Nb 44
3.2 Cellular Automata Modelling 46
3.2.1 Stainless Steel 316L 48
3.2.2 Ti34Nb 50
3.2.3 Conversion of Euler Angles to IPS Colouring 51
3.3 Experimental Setup 52
Chapter 4 Results and Discussion 54
4.1 CA Model 54
4.1.1 Parallelization 56
4.2 Simulation and Experimental Data Comparisons 58
4.2.1 Stainless Steel 316L 58
4.2.2 Ti34Nb 64
4.3 Limitations and Challenges 68
Chapter 5 Conclusion & Future Works 71

5.1 Conclusion 71

5.1.1 Cellular Automata Model 71

5.1.2 Simulation and Experiment Data of stainless steel 316L manufactured using selective laser melting 71

5.1.2 Simulation of titanium-niobium alloy manufactured using selective laser melting 72

5.1.3 Limitations of CAFE Simulation Model 72

5.2 Future Work 73

5.2.1 Columnar to Equiaxed Transition of Stainless Steel 316L 74

5.3 List of Publications 79

References 80

Summary

The microstructure of the metal is formed in process when fabricated using additive manufacturing (AM). The microstructure determines the mechanical properties of the metal and being able to predict what microstructure would form would be beneficial. This research uses simulations to predict the grain structure. Powder bed fusion of metal using laser (PBF-L/M), often called selective laser melting (SLM), was simulated. Two models were developed, a finite element method (FEM) thermal model that translated the process parameter to temperature profiles of the moving melt pool and a cellular automata microstructure model that uses the temperature profile from the FEM model and simulate the grain growth resulting in a grain structure. Two materials, stainless steel 316L (SS 316L) and Ti34Nb, were simulated and validated with experiments. Simulated melt pool dimensions of both materials were close to experiment results. The grain structure of the SS 316L showed similar patterns found in experiments. The grain width of the Ti34Nb had some differences with experimental results likely due to the unmelted niobium causing nucleation sites that is not accounted for in the model. Simulation of both materials would require simulating multiple layers to properly relate to the electron backscatter diffraction (EBSD) results.

List of Figures

Figure 1-1 Flow chart of process parameters as input producing temperature as output for thermal model and grain structure as output for microstructure model. 3

Figure 2-1 Example of printing schematics of selective laser melting and direct energy deposition. 7

Figure 2-2 Solidification theory flowchart [12, 13]. 8

Figure 2-3 a) Undercooling results in a difference in free energy. b) Temperature evolution of a pure metal with solidification driven by undercooling. 11

Figure 2-4 a) Increase in solute concentration in the front of the tip of dendrite. b) Total undercooling the molten metal experiences. 13

Figure 2-5 a) Temperature and concentration of solid and liquid metal in the mushy zone. b) Temperature of melt ahead of the dendrite, liquidus temperature drops due to the buildup of solutes. 14

Figure 2-6 Examples of (clockwise from (a)) planar, cellular, columnar dendritic and equiaxed dendritic solidifications [18]. 15

Figure 2-7 a) Dendrite in the preferred growth direction outgrowing other dendrites. b) Dendrites of preferred direction aligning to heat flow. 20

Figure 2-8 Columnar grains in stainless steel, titanium alloy and Inconel 625 [29], d) increased magnification on the stainless steel shows cellular dendrites that grow across melt pools. 22

Figure 2-9 Different scales of microstructure modelling. 24

Figure 3-1 Sequentially coupled cellular automata-finite element loop. 40

Figure 3-2 Thermal conductivity and specific heat capacity of SS 316L used in finite element simulation [110]. 43

Figure 3-3 Density of SS 316L used in finite element simulation [110]. 43

Figure 3-4 Thermal conductivity and specific heat capacity of Ti34Nb used in finite element simulation. 45
Figure 3-5 Density of Ti34Nb used in finite element simulation. 45
Figure 3-6 Different neighbourhood patterns in CA, grey cells are the neighbours of black cell. 46
Figure 3-7 Representation of the simulated tracks, where three combined tracks are simulated for each layer and rotated 90° in the second layer. Red arrows are tracks in the first layer and blue arrows are tracks in the second layer. 48
Figure 3-8 Plot of the dendrite growth velocity against undercooling temperature of SS 316L .. 49
Figure 3-9 Plot of dendrite growth velocity against undercooling temperature of Ti34Nb. 51
Figure 3-10 a) Schematic representation of the scanning strategy termed as “combined track” which consists of meandering short scans b) Microscope image of the stainless steel part printed using the scanning strategy. 53
Figure 4-1 On the left a single dendrite grown in constant temperature and on the right a single dendrite grown in a temperature gradient. 55
Figure 4-2 Two models showing the difference in using decentered square method. 56
Figure 4-3 Example of array being split for parallelization. 57
Figure 4-4 Example of arrays being padded and transferring of data to surrounding models. 58
Figure 4-5 Efficiency of parallel models for a given model. 58
Figure 4-6 Grain patterns seen in selective laser melted SS 316L part. Optical image obtained across the x-z plane of printed cube. 59
Figure 4-7 Measured melt pool dimensions in a) printed sample and b) FEA simulation. 60

Figure 4-8 Simulated grain structure of a single combined track, viewed from a) top view, b) cross section. IPF-maps shown have the crystallographic orientations relative to the building direction. 61

Figure 4-9 Top: Simulated grain structure in 3D with 3 combined tracks per layer for 2 layers, bottom: cross section of two planes showing the grain orientations. IPF-maps shown have the crystallographic orientations relative to the building direction. 63

Figure 4-10 a) shows the scanning strategy applied to the FEM model, b) shows the melt pool shape and moving direction for high laser power and c) shows the melt pool shape and direction for low laser power. 65

Figure 4-11 Grain width distribution of both simulation and experiment for case 1. 66

Figure 4-12 Grain width distribution of both simulation and experiment for case 2. 66

Figure 4-13 Comparison of EBSD and simulated results of printed Ti34Nb for both cases. The scale for the EBSD and simulated results are different. EBSD data is taken from Huang *et. al.* [108]. 67

Figure 5-1 Columnar to equiaxed transition of SS 316 [129]. 74

Figure 5-2 Illustration of the chessboard scanning strategy where each line is a single track scan. 76

Figure 5-3 Sampled data points from four cases plotted with the CET curve. 77

Figure 5-4 Sampled data of four laser rescanning cases plotted with the CET curve. 78

List of Tables

Table 2-1 Comparison of capabilities between microstructure models: kinetic Monte Carlo, cellular automata and phase field modelling. 36

Table 3-1 Parameters used for SS 316L in finite element simulation. 44

Table 3-2 Parameters used for Ti34Nb in finite element simulation. 46

Table 3-3 Parameters used for cellular automata simulation of SS 316L 49

Table 3-4 Parameters used for cellular automata simulation of Ti34Nb. 50

List of Abbreviations

Abbreviations	Full Terms
AM	Additive Manufacturing
AMR	Adaptive Mesh Refinement
CA	Cellular Automata
CAFE	Cellular Automata-Finite Element
CET	Columnar to Equiaxed Transition
CFD	Computational Fluid Dynamics
DED	Directed Energy Deposition
EBM	Electron Beam Melting
FDM	Finite Difference Method
FEM	Finite Element Method
FVM	Finite Volume Method
HCP	Hexagonally Closed Pack
IN	Inconel
MC	Kinetic Monte Carlo
PFM	Phase Field Modelling
SLM	Selective Laser Melting
SS	Stainless Steel

Nomenclature

Symbol	Description
α	Thermal diffusivity
A	Absorptivity of laser on substrate
c	Concentration of solute
c_p	Specific heat capacity
C_0	Nominal solute concentration of an alloy
$C^{l\,s/l}$	Liquid concentration at the solid/liquid interface
$C^{s\,s/l}$	Solid concentration at the solid/liquid interface
δ	Kronecker delta
d	Powder layer thickness
D^l	Solute diffusion coefficient
ε	Emissivity
$\emptyset$	Porosity
ΔE	Overall energy in a system
E_d	Energy density
F	Total free energy in a system
$\gamma^{s/l}$	Solid and liquid interfacial energy
Γ	Gibbs-Thomson coefficient of alloy
ΔG_n^{heter}	Heterogeneous nucleation barrier
ΔG_n^{homo}	Homogeneous nucleation barrier
G_c	Solute concentration gradient

G_T^l	Temperature gradient of liquid at the interface
ΔH	Latent heat of fusion
h	Coefficient of heat convection
h_d	Hatch spacing
I_j	Spin of the site in a lattice
I_k	Spin of the neighbour in a lattice
J	Scaling factor of an energy system
k	Equilibrium solute distribution coefficient
k_B	Boltzmann's constant
K	Thermal conductivity
λ_s	Minimum wavelength of moving interface
μ	Coefficient of kinetic undercooling
m^l	Gradient of liquidus slope
M_0	Arrhenius pre-exponential factor
M_c	Mobility of concentration field at the interface
M_ϕ	Mobility of phase field at the interface
n	Grain density
n_{max}	Maximum nucleation density
N_i	Number of nucleation sites of a certain area
N_0	Total heterogeneous nucleation site per unit volume
Ω_c	Dimensionless supersaturation
Ω_t	Dimensionless undercooling

ϕ	Phase
ϕ_v	Volume fraction
P	Power of energy source
P_t	Thermal Peclet number
P_c	Solutal Peclet number
Q	Heat input of energy source
Q_{act}	Activation energy
ρ	Density
r_0	Laser beam radius
R	Dendrite tip radius
R_{gas}	Gas constant
Δs_f	Specific entropy of fusion
θ	Phase fraction
t	Time
T	Temperature
T_0	Ambient temperature
T_{melt}	Temperature of the melt pool in front of the dendrite
T^l	Liquidus temperature in front of the dendrite
$T^{l\infty}$	Average temperature of melt pool
$T^{s/l}$	Temperature of the interface
ΔT	Undercooling temperature
ΔT_C	Solutal undercooling temperature

ΔT_K	Kinetic undercooling temperature
ΔT_m	Freezing range of alloy
ΔT_{mean}	Mean undercooling temperature
ΔT_R	Curvature undercooling temperature
ΔT_T	Thermal undercooling temperature
ΔT_σ	Standard deviation of undercooling temperature
v	Velocity of dendrite tip
v_e	Velocity of equiaxed dendrite growth
v_l	Scanning velocity
V	Volume
σ	Stefan-Boltzmann constant

Chapter 1 Introduction

1.1 Background

Additive manufacturing (AM) is a process that builds parts by addition of material layer by layer. AM grants greater geometric freedom, this allows for complex designs that conventional manufacturing are unable to achieve [1, 2]. Current AM process for metals uses either of the two general methods: powder bed fusion (PBF) and directed energy deposition (DED). Some common alloys that are additively manufactured include titanium, nickel and iron alloys [3-5]. The performances of these alloys are dependent on their microstructure.

The grain structure formed during the manufacturing process would determine the mechanical properties of the part. Grains that are smaller in size would lead to higher yield strength and increased ductility [6]. Grains with aspect ratio close to unity have isotropic properties while high aspect ratio grains are stronger in one direction causing anisotropy. Grains with high aspect ratio are called columnar grains and grains with aspect ratio close to unity are called equiaxed grains. The grain structure formed during AM process depends largely on the material and process parameters.

PBF of metal using laser as the energy source, which is also called selective laser melting (SLM), is common as it offers a variety of metals that can be fabricated [7]. Being able to predict the grain structure for different metals fabricated using SLM can be useful especially when exploring new process parameters and materials.

1.2 Significance of the Problem and its Challenges

The microstructure of the metal can give insights to mechanical properties as well as possible failure mechanisms [8, 9]. Predicting grain structures can be particularly useful in getting the amount of anisotropy the bulk material would exhibit. Grain structure can be found by fabricating the metal and carrying out material characterization. However, fabricating metal by SLM can be expensive due to the high cost of powders, high power usage, requirement of multiple ancillary equipment and consumables [7]. Experimenting with different process parameters might lead to failed builds which can damage consumables and require time to clean and prepare the machine for fabrication again.

Simulations can be used to predict grain structures in place of carrying out multiple experiments, thereby reducing cost and time. Simulations just require a computer preferably with fast processing speed or for more intensive simulations, computers with multiple cores or even multiple processors. Simulations are not without disadvantages; they often require some assumptions that results in some difference between simulation and experiments. Physics based simulation often require longer time and larger amount of computational resources as compared to statistical based simulation. Even with these disadvantages, as simulations require only computer and time, it can be more accessible, cheaper and more environmentally friendly as compared to running the same number of experiments.

1.3 Objectives and Scope

The objective of this research is to get a working simulation model that is able to take certain process parameters and predict the thermal profile and grain structure for the SLM process as shown in Figure 1-1. The process parameters that are considered are the laser power, laser profile,

scanning speed, scanning strategy and layer thickness. This is because the energy density (Equation 2.1), which is detailed in Section 2.1, is often used to classify the parameters use to quantify the energy input in each scan and consist of the laser power, scanning speed, layer thickness and hatch spacing. The scanning strategy affects how the energy is input over time and the hatch spacing. The laser profile is limited to what is calibrated for in the machine.

The output for thermal profile should be able to provide the temperature profile giving information on melt pool width, depth and cooling rate. The output for the microstructure model should be able to have a good indication on the grains form and its evolution as a melt pool moves across model.

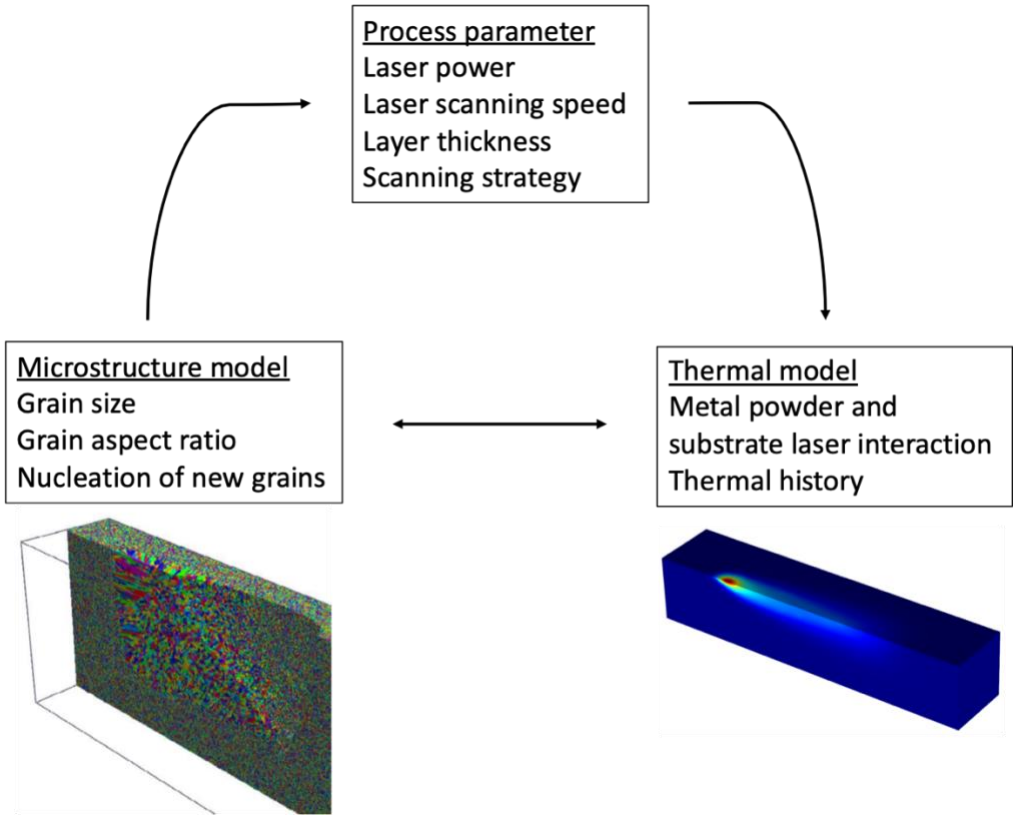

Figure 1-1 Flow chart of process parameters as input producing temperature as output for thermal model and grain structure as output for microstructure model.

1.4 Potential Contributions

This research contributes to developing simulation models that can readily simulate a variety of metals fabricated using SLM that can aid in getting process parameters that lead to desirable grain structure. This could be applied by getting a set of process parameters before running expensive experiments, trying new process parameters that can lead to a change in grain structure and using the simulated models to explain grain structures observed in experiment data. Furthermore, simulations that consider scanning strategies have not been developed. In this research, a simulation model that can predict grain structures in multi-layer with different scanning strategies was developed.

1.5 Organization of Report

This report consists of five chapters. The first chapter gives the background of metals in AM, AM processes, microstructure of AM metals, the motivations and objectives of this research.

Chapter 2 reviews literature on AM methods for metal, grain structure of AM metals, solidification theory and simulation techniques use for microstructure models.

Chapter 3 summarises the methodology used in this research. This includes the parameters used in the simulation as well as the material properties used for calculation. The equations used in finite element method and cellular automata were reviewed. The rules of cellular automata and coupling of the two methods are discussed as well.

Chapter 4 discusses how the cellular automata model was coded, the thermal and microstructure simulations done for stainless steel and titanium-niobium alloy, the comparison between simulated

data and experimental data fabricated using SLM. The limitations and challenges were discussed as well.

Lastly, Chapter 5 concludes the research done and summarises the possible future work for this research.

Chapter 2 Literature Review

This chapter reviews the AM methods for metals specifically PBF and DED. The grain structure that AM metal typically exhibit and the methods used to change the grain structure are reviewed. Lastly, numerical models that are used for grain structure simulation are reviewed. The models are classified as thermal and microstructure models. The two classes of models are coupled together during simulations.

2.1 Additive Manufacturing Methods for Metals

Two common groups of additive manufacturing techniques for fabricating metals are PBF and DED (Figure 2-1). PBF of metal commonly uses laser or electron beam as energy source for melting. They are also commonly called selective laser melting (SLM) and electron beam melting (EBM), respectively. Both SLM and EBM start from digital data such as a 3D model which is then sliced into layers and sent to the machine. The fabrication process is often automated, starting from deposition of powder onto the powder bed and spread evenly across. Then, the energy source melts the powder to form a layer of solid metal that bonds with the substrate or previously melted structure. This is repeated till all the layers are deposited and melted.

DED process has the material fed either by wire or by blowing powders to the melt pool. The energy source could either be laser or electron beam. DED process often uses a laser of larger diameter compared to PBF, allowing faster build of large objects at the sacrifice of resolution. The process parameters are similar to PBF process but with some additional parameters like feed rate and nozzle offset distance.

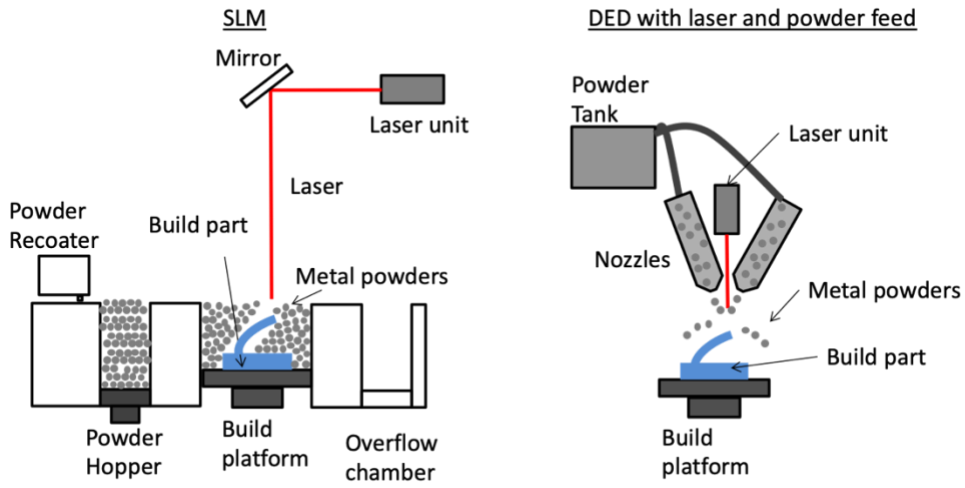

Figure 2-1 Example of printing schematics of selective laser melting and direct energy deposition.

The process parameters of each AM method determines the success of the fabrication and thus are most often experimented with to determine the optimal print settings [10]. Some common parameters are power of the energy source, scanning speed of the energy source, layer thickness, hatch spacing and scanning strategy. A common term to describe these parameters is by the energy density which is computed by:

$$E_d = \frac{P}{v_l h_d d}, \tag{2.1}$$

where P is the power of the energy source, v_l is the scanning velocity, h_d is the hatch spacing and d is the layer thickness. Energy density is commonly used to determine optimal setting to obtain minimum porosity. Different scanning strategies results in differing residual stress and deformation [11]. All these parameters affect the melting, cooling and solidification rates and would therefore determine the final microstructure of the built part.

2.2 Grain Structure of Additively Manufactured Metals

This section first reviews the relevant theory required for CA modelling of AM processes. It would start firstly from nucleation which is the beginning of the solidification process. Secondly, the

undercooling which is the driving force of solidification is reviewed. Thirdly, the dendritic growth where the dendrite size and growth speed are reviewed. Fourth, the grain structure in SLM is studied which completes the analyses of the solidification process. Lastly, the grain structure observed from metals fabricated using SLM.

2.2.1 Theory of Solidification

As molten metal cools, it changes state from liquid to solid, and the way it solidifies would determine its microstructure. An example of the solidification is first it starts off from nucleus and as the melt pool cools lower than the liquidus temperature they grow into dendrites. As the melt pool moves, the dendrite grows larger and longer and when multiple dendrites are oriented in the same direction it could become grain. Multiple grains forming together to a single solid would lead to a polycrystalline metal (Figure 2-2).

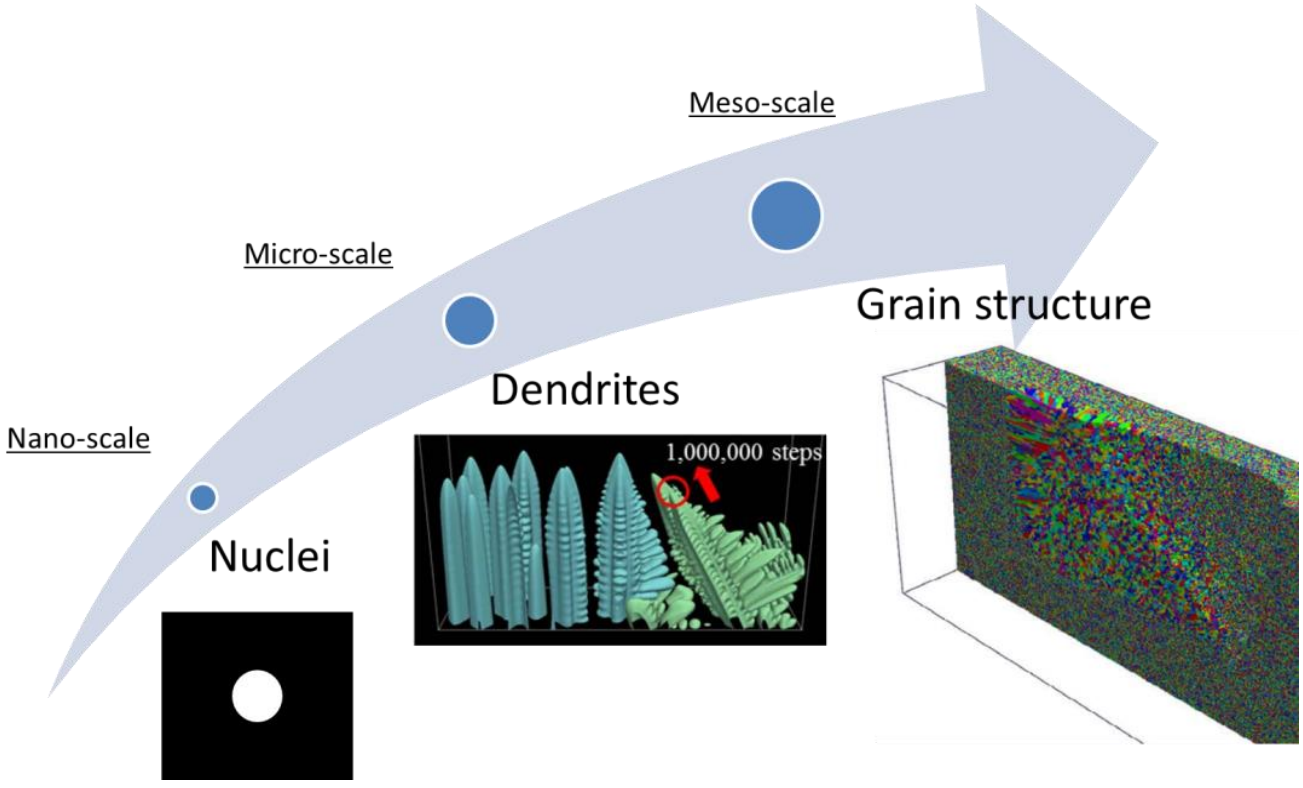

Figure 2-2 Solidification theory flowchart [12, 13].

2.2.1.1 Nucleation

For a crystalline solid, nucleation occurs randomly in the molten metal to give the first step of solidification. Nucleation is the formation of a cluster of atoms that align in a crystalline structure [14]. If the clusters are too small, the clusters would return to its liquid state and are called embryos. Clusters that are large enough to remain stable are called nuclei. The nuclei can form into two kinds of nucleation, homogeneous and heterogeneous nucleation. For pure material, the melt would nucleate homogeneously while in materials that have impurities or have alloying components, the melt would likely nucleate heterogeneously.

The driving force of homogeneous nucleation is the free energy at the solid/liquid interface of both the liquid and solid. In order for a cluster to achieve critical size to be stable, it requires to have large enough free energy called the homogeneous nucleation barrier [14]:

$$\Delta G_n^{homo} = \frac{16\pi}{3}\frac{(\gamma^{s/l})^3}{(\rho \Delta s_f \Delta T)^2}, \tag{2.2}$$

where $\gamma^{s/l}$ is the solid and liquid interfacial energy, ρ is the density, Δs_f is the specific entropy of fusion and ΔT is the undercooling. Heterogeneous nucleation occurs when there are foreign particles or on the surface of the mould which are different material than the melt. The cluster would form on the foreign surface and depending on the wetting angle of the melt on the surface, the heterogeneous nucleation barrier can be found:

$$\Delta G_n^{heter} = \Delta G_n^{homo} \cdot f(\theta_w), \tag{2.3}$$

$$f(\theta_w) = \frac{1}{4}(2 + \cos\theta_w)(1 - \cos\theta_w)^2, \tag{2.4}$$

where θ_w is the wetting angle and $f(\theta_w) \in [0,1]$ is a geometric factor dependant on the volume of the droplet as compared to a full sphere.

When $\theta_w = \pi$, $f(\theta_w) = 1$, the melt is non-wetting, and the heterogeneous nucleation barrier is equalled to the homogeneous nucleation barrier as the melt becomes a sphere. On the other hand, when $\theta_w = 0$, $f(\theta_w) = 0$, the melt is perfectly wetting and there is no nucleation barrier. This happens when the material of the melt is the same as the foreign particle. In the SLM process, the melt pool experiences nucleation on the substrate or previously melted layer, which is the same material, leading it to an epitaxial solidification, where $\Delta G_n^{heter} = 0$.

2.2.1.2 Undercooling

When the molten metal is above the melting temperature, the free energy of the liquid would be lower than that of the solid. Similarly, the free energy of the solid is lower than that of the liquid when the molten metal is lower than the melting temperature (Figure 2-3a). The free energy of the metal would want to be minimised and tend to go to the state of lower energy. The difference in free energy drives solidification and this is seen when metal solidifies at temperature cooler than the liquidus temperature, also called undercooling. Undercooling is the difference between the temperature of the melt pool just ahead of the dendrite and the melting temperature (Figure 2-3a). For pure metals, at the melting point, both liquid and solid phases have the same free energy and both states can exist in equilibrium. Therefore, undercooling is essential to drive the nucleation process. For alloys, the undercooling is the temperature difference between the molten metal and the liquidus temperature. As metal solidifies, the temperature does not change as heat is released by latent heat. And only once the metal fully solidifies, the temperature continues to drop (Figure 2-3b). As most metals being fabricated are alloys, from this point forwards undercooling would be

assumed to the liquidus temperature minus the temperature of the molten metal just ahead of the dendrite.

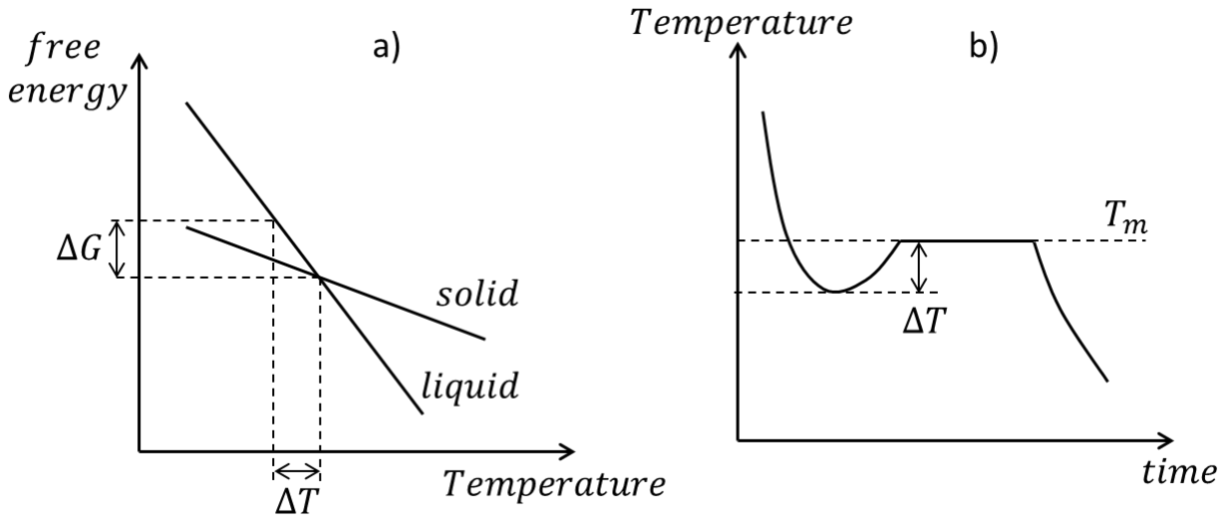

Figure 2-3 a) Undercooling results in a difference in free energy. b) Temperature evolution of a pure metal with solidification driven by undercooling.

The total undercooling is determined by adding four types of undercooling, thermal, solutal, curvature and kinetic:

$$\Delta T = \Delta T_T + \Delta T_C + \Delta T_R + \Delta T_K \, . \tag{2.5}$$

The thermal undercooling, ΔT_T, is the difference between the temperature at the interface, $T^{s/l}$, and the average temperature of the melt, $T^{l\infty}$.

$$\Delta T_T = T^{s/l} - T^{l\infty} \, . \tag{2.6}$$

The curvature undercooling, ΔT_R, is due to the Gibbs-Thomson effect. The radius of the solid surface would reduce the melting temperature and the undercooling for a dendrite tip can be estimated by the Gibbs-Thomson coefficient of the alloy, Γ, and radius of the tip, R [15].

$$\Delta T_R = \frac{2\Gamma}{R}. \tag{2.7}$$

The kinetic undercooling, ΔT_K, is the velocity of the solid surface, υ, divided by the coefficient of kinetic undercooling, μ. As μ is in the order of 10^{-2} $mK^{-1}s^{-1}$ [16], kinetic undercooling would become significant only if the growth rate is in the range of meters per second.

$$\Delta T_K = \frac{\upsilon}{\mu}. \tag{2.8}$$

Solutal undercooling or constitutional undercooling, ΔT_C, is the undercooling due to concentration difference between the solid surface and the liquid in an alloy. For pure metals, the solutal undercooling is zero. There are three cases in which solutal undercooling would take place. First is when there is complete diffusion between and within both the solid and liquid during equilibrium solidification. Second is when there is no diffusion in the solid while there is complete diffusion in the liquid. The first case requires extremely slow solidification rates and the second case requires very large convection currents in the liquid melt. Since SLM has similar solidification conditions as welding, these two cases would unlikely happen in SLM [17]. The third case which is most relevant to SLM is when there is no diffusion in the solid and limited diffusion in the liquid. This means that as the solid grows, the solute in the liquid is rejected and the concentration of the solute increases at the liquid interface. The solute rich boundary ahead of the growth causes the liquidus temperature to drop as shown in Figure 2-4a. If the temperature of the melt, T_{melt}, at the solute rich region is lower than the liquidus temperature, T^l, the undercooling is the difference between them (Figure 2-4b). The solutal undercooling is then the difference between the liquidus temperature and the actual melt temperature:

$$\Delta T_{C(x)} = T^l(x) - T_{melt}(x), \tag{2.9}$$

For a binary alloy, the solutal undercooling can be estimated base on the phase diagram where C_0 is the nominal solute concentration, $C^{s\,s/l}$ is the solid concentration at the solid/liquid interface, $C^{l\,s/l}$ is the liquid concentration at the interface and k is the equilibrium solute distribution coefficient [15].

$$k = \frac{C^{s\,s/l}}{C^{l\,s/l}}\,. \tag{2.10}$$

From the phase diagram, the solid and liquid concentration of the solute, as well as the solidus and liquidus temperature, can be found, based on the nominal solutal concentration of the solute in the melt (Figure 2-5).

$$\Delta T_C = m^l\left(C_0 - C^{l\,s/l}\right), \tag{2.11}$$

where m^l is the gradient of the liquidus slope in the phase diagram as shown in Figure 2-5b.

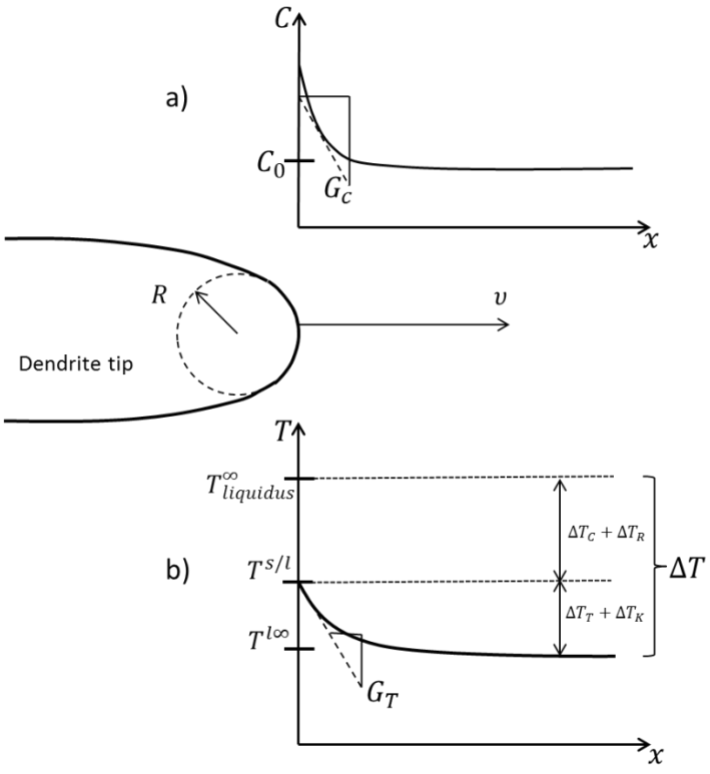

Figure 2-4 a) Increase in solute concentration in the front of the tip of dendrite. b) Total undercooling the molten metal experiences.

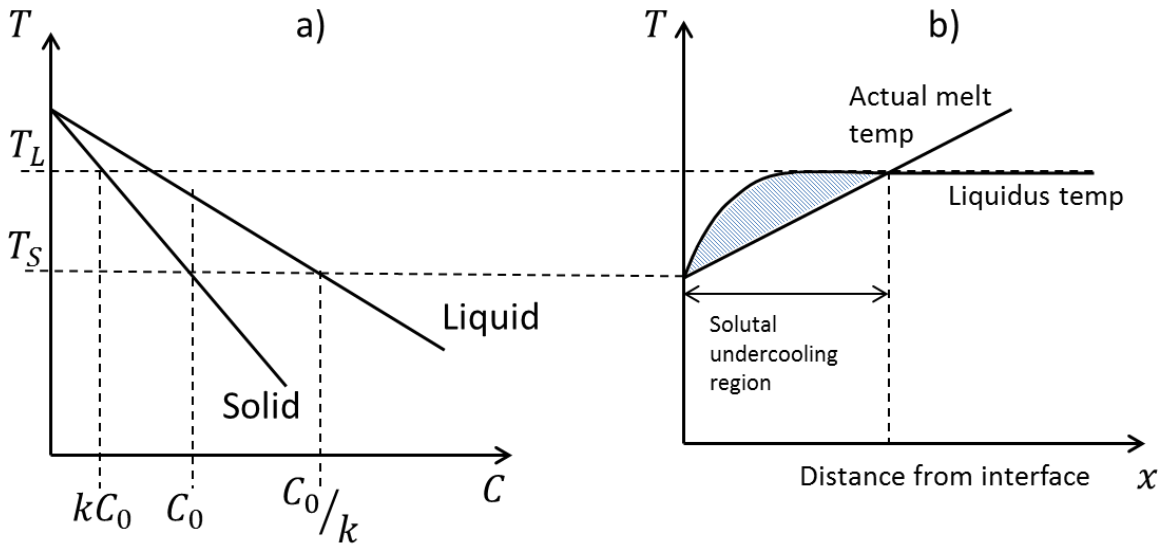

Figure 2-5 a) Temperature and concentration of solid and liquid metal in the mushy zone. b) Temperature of melt ahead of the dendrite, liquidus temperature drops due to the buildup of solutes.

2.2.1.3 Dendritic Growth

There are three kinds of grain growth that can happen: planar, cellular and dendritic (Figure 2-6). Depending on the thermal gradient and interface growth velocity, different grain structures would form. For the SLM process, the melt is interfacing with a similar material leading to epitaxial growth. The microstructure formed during the growth depends on the stability of the solid/liquid interface.

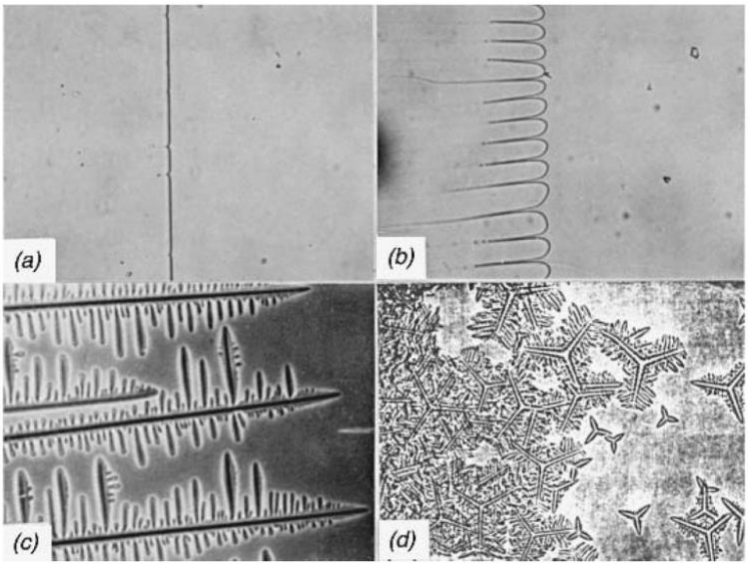

Figure 2-6 Examples of (clockwise from (a)) planar, cellular, columnar dendritic and equiaxed dendritic solidifications [18].

For pure metals, the temperature gradient of the liquid at the interface, G_T^l, controls the stability. When G_T^l is positive, the solidification is planar and when G_T^l is negative, the interface becomes unstable and leads to dendritic or cellular growth instead. However, for alloys, the temperature gradient alone is not enough to analyse the stability of the interface. Flemings showed that even when G_T^l is positive, there are varying solidification morphologies [19]. The stability is also dependent on the velocity of the growth of the solid/liquid interface. Flemings found that at high values of $\frac{G_T^l}{v}$, the solidification growth was planar and at low values, columnar or equiaxed dendrites formed instead. The stability criterion of the solidification plane for solutal undercooling is [20]:

$$\frac{G_T^l}{v} \geq \frac{\Delta T_m}{D^l}, \tag{2.12}$$

where ΔT_m is the freezing range of the alloy and D^l is the solute diffusion coefficient. If equation 2.12 is satisfied, the solidification is planar. In order for this to happen, the growth of the interface

has to be slow. As such, for the solidification process of SLM which has high cooling rates, dendritic growth is most likely to happen.

Dendrite structures are tree-like and are characterised by its growth direction, dendrite tip radius, primary spacing and higher order arm spacing. Dendritic growth arises from an undercooled melt ahead of the tip. The tip can be described as a parabolic shape in 2D and paraboloid in 3D growing at a constant velocity [21]. Ivantsov developed solutions for the diffusion field around a dendrite tip that satisfy the shape preserving condition [22]. The Ivantsov function, Iv(P), is applicable for both the thermal and solutal fields:

$$\mathrm{Iv}(P_t) \equiv \Omega_t = P_t \exp(P_t)\, E_1(P_t)\,, \tag{2.13}$$

$$P_t = \frac{vR}{2\alpha}\,, \tag{2.14}$$

$$\mathrm{Iv}(P_c) \equiv \Omega_c = P_c \exp(P_c)\, Ei(P_c)\,, \tag{2.15}$$

$$P_c = \frac{vR}{2D^l}\,, \tag{2.16}$$

$$E_1(P) = \int_P^{\infty} \frac{e^{-x}}{x}\, dx\,, \tag{2.17}$$

where Ω_t is the dimensionless undercooling, P_t is the thermal Peclet number, E_1 is the exponential integral function, α is the thermal diffusivity, Ω_c is the dimensionless supersaturation and P_c is the solutal Peclet number. According to Ivantsov, the dimensionless undercooling is proportionate to the thermal undercooling and the dimensionless supersaturation is the difference between the

liquid concentration and nominal concentration divided by the difference between the nominal concentration and the solid concentration at the solid/liquid interface:

$$\Omega_t = \frac{\Delta T_T c_p}{\Delta H}, \tag{2.18}$$

$$\Omega_c = \frac{C^{l\,s/l} - C_0}{C^{l\,s/l}(1-k)}, \tag{2.19}$$

where c_p is the heat capacity and ΔH is the latent heat of fusion. Combining equations 2.5 to 2.8, 2.11, 2.13, 2.15, 2.18 and 2.19 would give the undercooling equation:

$$\Delta T = \frac{\Delta H}{c_p} Iv(P_t) + m^l C_0 \left(1 - \frac{1}{1-(1-k)Iv(P_c)}\right) + \frac{2\Gamma}{R} + \frac{v}{\mu}. \tag{2.20}$$

The total undercooling is shown in Figure 2-4b. The set of equations 2.13 to 2.20 would give a solution in terms of Peclet numbers, or in terms of vR. In order to get the undercooling in terms of v and R, another equation is required. Langer and Müller proposed that the dendrite tip grows close to a steady state which they termed marginally stable [23]:

$$R = \lambda_s, \tag{2.21}$$

where λ_s is the minimum wavelength at the growing interface. Lipton *et al.* adopted the marginally stable criterion that Langer proposed for low Peclet numbers (LGK method) [15]:

$$R = \sqrt{\frac{4\pi^2\Gamma}{m^l G_c - G_T^l}}, \tag{2.22}$$

$$G_c = -\frac{2P_c C_0(1-k)}{R}, \tag{2.23}$$

$$G_T^l = -\frac{2P_t\Delta H}{c_p R}, \tag{2.24}$$

$$R = \frac{4\pi^2\Gamma}{\frac{P_t\Delta H}{c_p} - \frac{P_c m^l C_0(1-k)}{1-(1-k)Iv(P_c)}}, \tag{2.25}$$

where G_c is the solute concentration gradient in the liquid of the interface. Combining equations 2.20 and 2.25 would give unique values of the interface growth velocity and dendrite tip radius for a given undercooling. Trivedi and Kurz later extended the work of Langer and Müller to find the stability of the interface and high Peclet numbers [24]. Lipton *et al.* extended the LGK method to include high Peclet numbers (LKT method) [25]. With the assumption that the tip is isothermal and there is equal thermal diffusivity, the radius can be described as:

$$R = \sqrt{\frac{4\pi^2\Gamma}{m^l G_c \xi_c - G_T^l \xi_t}} = \sqrt{\frac{4\pi^2\Gamma}{\frac{P_t\Delta H}{c_p}\xi_t - \frac{2P_c m^l C_0(1-k)}{1-(1-k)Iv(P_c)}\xi_c}}, \tag{2.26}$$

$$\xi_c = 1 + \frac{2k}{1-2k-\sqrt{1+\frac{4\pi^2}{{P_c}^2}}}, \tag{2.27}$$

$$\xi_t = 1 - \frac{1}{\sqrt{1+\frac{4\pi^2}{{P_t}^2}}}. \tag{2.28}$$

At large Peclet numbers, the functions ξ_c and ξ_t can be approximated to:

$$\xi_c \cong \frac{\pi^2}{kP_c^{\,2}}, \tag{2.29}$$

$$\xi_t \cong \frac{2\pi^2}{P_t^{\,2}}. \tag{2.30}$$

It can be seen that Equations 2.27 and 2.28 tend towards one when Peclet numbers are small, which would cause Equations 2.26 and 2.25 to be equal.

Kurz *et al.* also used the marginally stable criterion for directional solidification which has a fixed thermal gradient where the radius can be described as (KGT method) [26]:

$$R = \sqrt{\frac{4\pi^2\Gamma}{m^l G_c \xi_c - G_T^l}}. \tag{2.31}$$

This is similar to Equation 2.25 with the thermal function, ξ_t, equals to one. This is true for some metals with very high thermal diffusivity leading to low thermal Peclet numbers.

The equations for the solutal undercooling above is only true for binary alloys, for alloys with more solute elements, the solutal undercooling would be:

$$\Delta T_C = \sum_{i=1}^{n} m_i^l C_{0\,i}\left(1 - \frac{1}{1-(1-k)Iv(P_c)}\right), \tag{2.32}$$

$$P_{c\,i} = \frac{vR}{2D_i^l}, \tag{2.33}$$

$$R = \sqrt{\frac{4\pi^2\Gamma}{\sum_{i=1}^{n} m_i^l G_{c\,i}\xi_{c\,i} - G_T^l\xi_t}}, \tag{2.34}$$

where i represent the solute elements and n is the number of solute elements, for a binary alloy $n = 1$.

2.2.1.4 Grain Structure

The grain growth of dendrites is biased towards a certain direction. For cubic metals, the preferred direction is $< 100 >$ and for hexagonal closed pack (HCP) metals the preferred direction is $< 10\bar{1}0 >$ [18]. In the preferred direction, dendrites grow faster, often out-competing dendrites of other directions, thereby stopping their growth (Figure 2-7a). The grains would also tend to grow in the same direction as the temperature gradient. As the grain grows, the grains that are oriented along the temperature gradient and in the preferred crystallographic direction would outgrow the other crystals thereby stopping their growth (Figure 2-7b).

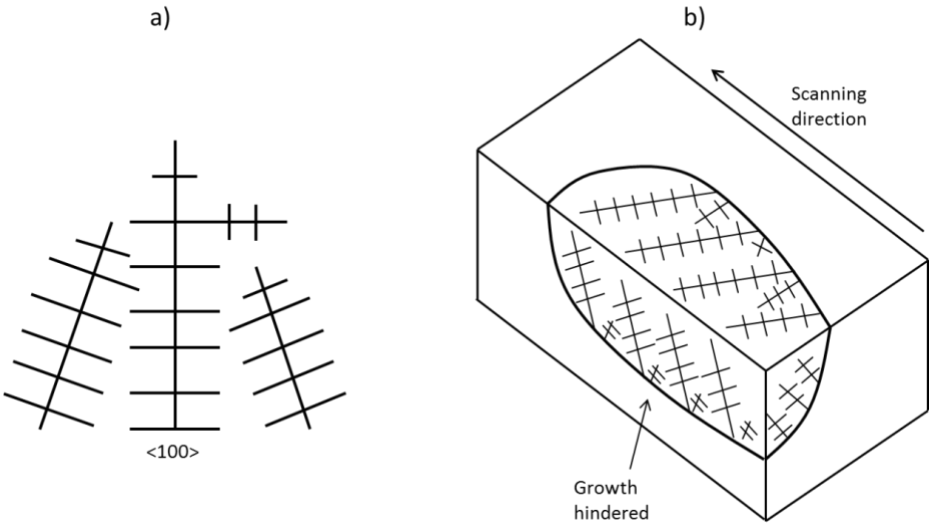

Figure 2-7 a) Dendrite in the preferred growth direction outgrowing other dendrites. b) Dendrites of preferred direction aligning to heat flow.

During the SLM process, the melt pool can nucleate from the bottom and the sides. The bottom could be either the substrate or a previously melted layer and the sides would be previously melted track in the same layer. As such solidification starts from partially melted layers at the bottom and sides, nucleation would first determine the grain structure. Beyond the partially melted area, grain growth would dominate the grain structure. In an epitaxial growth, the melt solidifies from existing crystal structures, adopting the direction of the existing crystals and growing in the same direction. This can lead to columnar grains along the laser direction as well as along the build direction [27].

2.2.2 Experimental Observations of Additively Manufactured Metals

Grain structures affects the mechanical properties of the printed parts and it is useful to understand how process parameters for each technology can influence the final printed grain structure [6, 28]. AM processes predominantly produce columnar grains along the build direction with a mixed of equiaxed grains in the printed parts (Figure 2-8) [29-31]. A printed part largely composed of columnar grains can show anisotropy leading to difference in strength at different directions [32]. Given the same material, the grain structure can change by varying the energy sources and feed types [31].

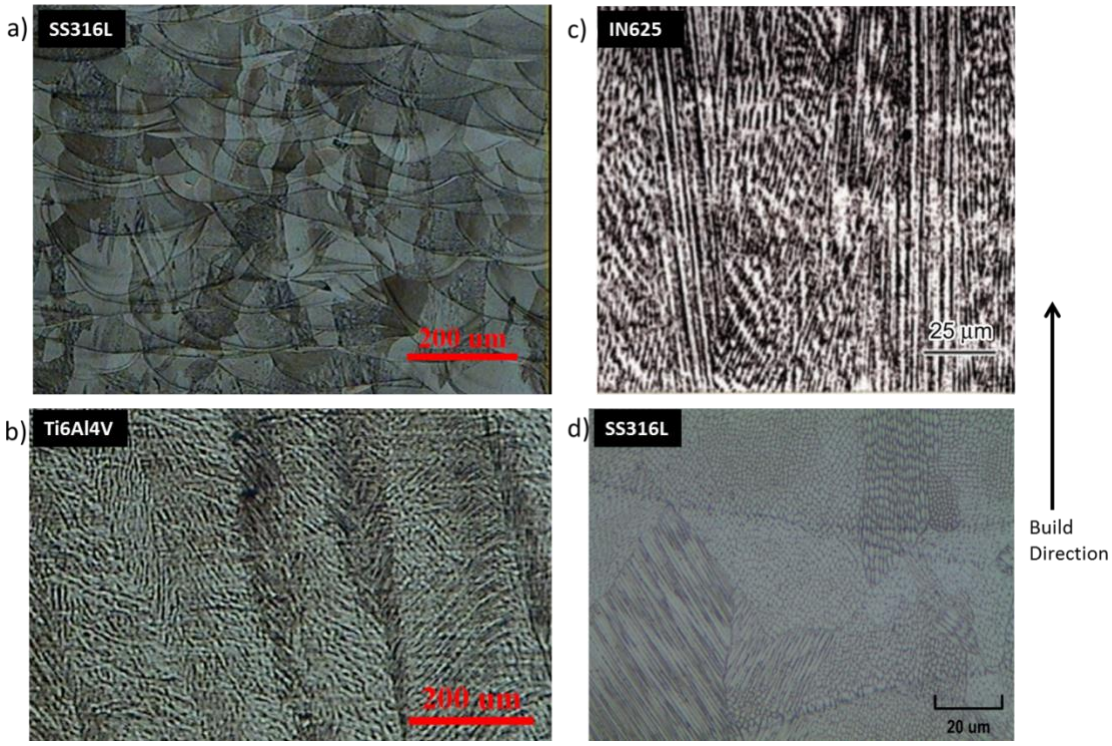

Figure 2-8 Columnar grains in stainless steel, titanium alloy and Inconel 625 [29], d) increased magnification on the stainless steel shows cellular dendrites that grow across melt pools.

Grain structure is formed during solidification and is thus largely determined by the material, thermal gradient and cooling rate. Without changing the material, grain structure is heavily influenced by the process parameters. Raghavan *et al.* used pulsed laser instead of continuous laser to alter the grain structure of Inconel 718 using SLM [33]. A different scanning strategy was used as well in order to ensure sufficient cooling between each laser pulse, allowing the grain structure to transit from columnar to equiaxed. Dehoff *et al.* used varying scanning speeds to alter the melt pool shape thereby leading to different grain structures in Inconel 718 using EBM [34]. AM has the potential to print customized microstructure according to application needs. While grain structures have been shown to be altered in Inconel, there are little to no works done on other metals in AM. In order to print different grain structure, understanding the thermal and

microstructural change is important. There are two ways to study the grain structure for AM, experimental and by computer simulations.

Experimental methods can yield the most accurate results. However, they lack flexibility as the parts can only be characterized after fabrication. Experimenting multiple process parameters can also lead to increased cost, failed builds and is time consuming. Simulations on the other hand would help in reducing cost and can help in predicting thermal profile and grain structure before fabrication. The cost of running experiments depend largely on powder price as it tends to be most pricey running cost, depending on the percentage of platform and build space used, the cost per part can vary between Euro 10 to 100 (~USD 12 to 121) per stainless steel piece [35-37]. As this is a research project it would be very unlikely to fill the entire build space making the estimated price per piece to be closer to Euro 100. Moreover, stainless steel is relatively cheaper compared to other materials like titanium which would drive the cost of experimenting up. On the other hand, renting a supercomputer cost approximately around USD 0.10 to 0.20 per core per hour, simulating for one parameter would take 4 cores and 72 hours which would cost around USD 29 to 58.
However, unlike experiments, simulations often use assumptions causing discrepancies between simulation results and experimental results. Although less accurate, simulations provide a cost-effective way to examine multiple process parameters and is worth exploring.

2.3 Modelling of Microstructure for Additively Manufactured Metals

When considering simulation of microstructure, two models are required. A thermal model that is in the macro scale and a microstructure model that is in either a meso scale or micro scale (Figure 2-9). The thermal model is required to provide data on the temperature, temperature gradient and cooling rate. Microstructure model are coupled with the thermal model to then predict the final

part microstructure. A meso scale model would likely only predict the grains while a micro scale model can predict more data like dendrite size and solute concentration.

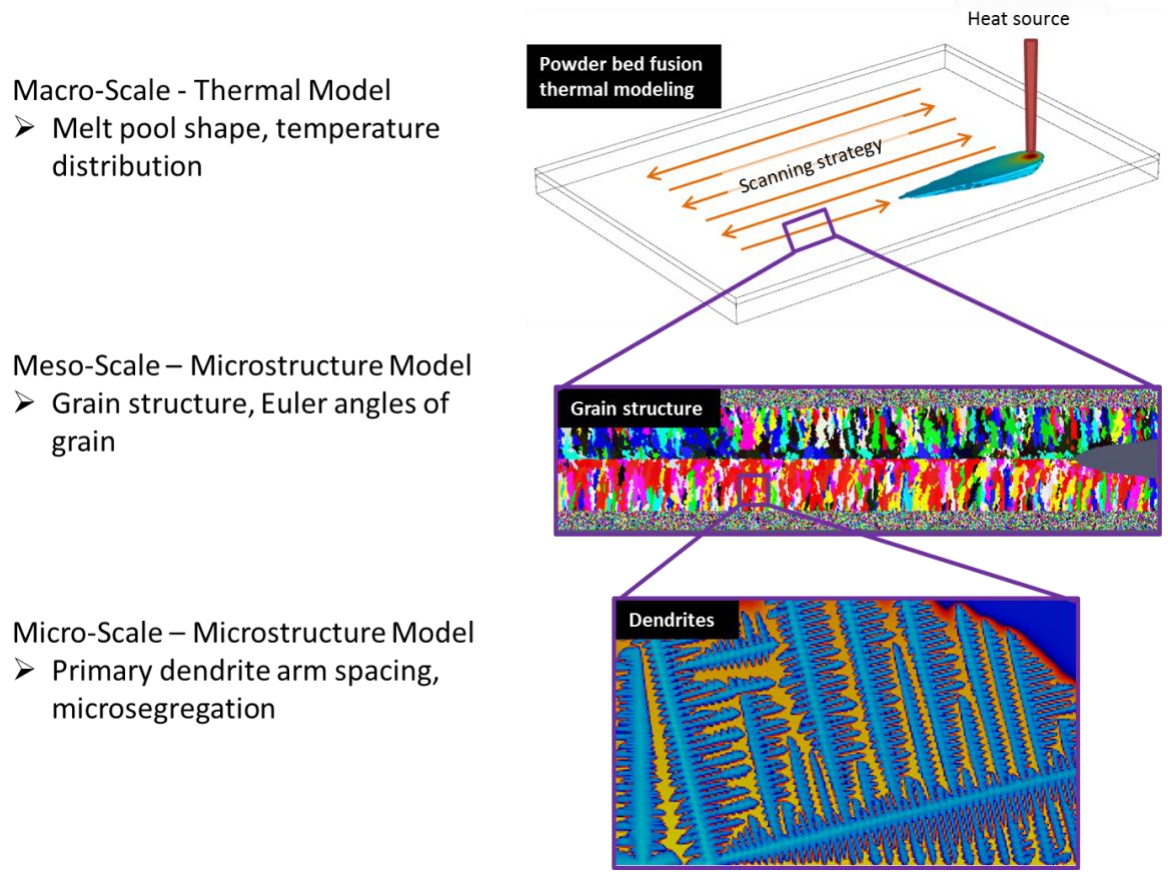

Figure 2-9 Different scales of microstructure modelling.

2.3.1 Thermal Models

2.3.1.1 Finite Difference Method and Finite Element Method

Two common models that simulates heat transfer without liquid flow is finite difference method (FDM) and finite element method (FEM). Both models have been used to couple with microstructure models [13, 38-40]. FEM/FDM get the temperature by solving the heat equation partial differential equation (PDE):

$$\rho c_p \frac{\delta T}{\delta t} - \nabla \cdot (\mathrm{K}\nabla \mathrm{T}) = \dot{\mathrm{q}}_V \,, \tag{2.35}$$

where ρ is the density, c_p is the specific heat capacity, T is the element temperature, t is the time, K is the thermal conductivity and lastly $\dot{q}_V$ is the volumetric heat source. Other effects such as convection and radiation are accounted for by applying a boundary condition at the surface or by modifying the material properties at certain temperature [41].

The PBF process have the first layer of powder spread over the substrate and the laser melts from the top of the powder layer. In order to simulate this, FEM models apply different material properties to the top powder layer and the bottom solid layer. This is because the powder layer is less dense and can lead to different thermal properties such as the thermal conductivity [13, 42, 43]. Often the elements assigned with powder material are change to solid material once it goes above the liquidus temperature as it can be safely assumed it has become solid.

The DED process differs from PBF in that powder is added while melting and solidification is occurring. In order to cope with this difference, the model can have the top powder layer set as a dead or inactive element which have its material property modified or have its variable fixed such as having the temperature of the dead element to be unchanged no matter what. The dead element is then set active when the heat source comes near it, simulating the addition of energy [44].

Meshing is an important topic in simulation of thermal models. The shape of the element can have effect on the accuracy and simulation speed. A common shape used in thermal model is the hexahedral shape, this is because often the model is a simple rectangular block instead of a complex shape. Hexahedral elements provide high accuracy and fast simulation speeds [45]. The size of the elements relative to the heat source is important, the element size should have sufficiently high resolution at the area of the heat source to estimate the temperature more

accurately. As a laser heat source in AM often range in the micron level, the element size has to be in the micro scale as well. This higher resolution required tends to cause long simulation times. Using an adaptive mesh sizing that is able to have micron sized elements only at the location near the heat source and progressively increase the element size away from the heat source would like to lesser element count and faster simulation speeds [46, 47].

2.3.1.2 Computational Fluid Dynamics

Unlike FEM, CFD models can simulate liquid flow in the melt pool which can lead to better temperature prediction. A common CFD method is the finite volume method (FVM) which solves the Navier-Stokes equation and is able to simulate the Marangoni effect and vaporization [48, 49]. The additional effects that it could simulate means higher geometrical and thermal accuracy [48]. FVM solves for the energy (Equation 2.36), mass conservation (Equation 2.37) and momentum (Equation 2.38) equations simultaneously [50, 51]:

$$\frac{\delta}{\delta t}(\rho H) + \nabla \cdot (\rho \vec{v} H) - \nabla \cdot (k \nabla T) = Q_S, \tag{2.36}$$

$$\frac{\delta \rho}{\delta t} + \nabla \cdot (\rho \vec{v}) = M_s, \tag{2.37}$$

$$\rho \frac{\delta \vec{v}}{\delta t} + \rho \vec{v} \cdot \nabla \vec{v} = -\rho \nabla p + \mu \Delta \vec{v} + M_s \vec{v} + F. \tag{2.38}$$

Where H is the enthalpies, $\vec{v}$ is the velocity of fluid, M_s is the mass source, μ is the dynamic viscosity and F is a force term like gravitational force that may be included. Simulating for PBF, the mass source is often zero as no mass is added during the melting process. In DED, powder or wire is added during in-process and mass source is non-zero.

Compared to FEM, FVM need to solve for more equations simultaneously in a single step leading to more data predicted and higher accuracy. This comes with a sacrifice on speed leading to most simulations to simulate a smaller scenario such as just a single track instead of a layer [48, 52-54]. An additional advantage FVM have is its able to replicate different powder distribution [55, 56]. Powder flow is important in DED process that uses powder as feedstock. Unlike wire, powder is affected by any gas flowing such as inert gas used for shielding. Discrete element modelling (DEM) is commonly used to simulate powder flow and have been coupled with CFD. DEM can be used to simulate the powder in flight from the nozzle to the energy source and CFD is coupled to simulate the heating and melting of the powder to form a solid on the substrate [57]. The increase in complexity also means there is an increase in computational resources required, slowing the CFD simulation further.

Another common CFD model is the Lattice Boltzmann method (LBM). LBM solves the discrete Boltzmann equations to model the flow of imaginary particles that represent the fluid in a lattice [58]. As LBM does not require solving multiple PDEs that FVM needs, it is also able to simulate powder distribution together with thermal and liquid flow in a single model [48, 59]. Most literature simulate 2D models for AM when using LBM, this might be due to the comparatively more expensive computational requirements when switching from 2D to 3D [60-62]. While FVM have been used to simulate both PBF and DED processes so far LBM have only been used to simulate PBF process.

CFD models provide high accuracy than FEM models but is relatively slower and often use to simulate for a single track. Simulating for varying process parameters including scanning strategy

would require simulating multiple tracks and even layers. In such a case where scanning strategy is of importance, FEM would make more practical sense.

2.3.2 Microstructure Models

There are similarities to be made when comparing the melting of metals in a welding and in AM process. The soldification process can be similar as in both cases, material is added to a base material and a heat source is used to melt the additional material to bond to the base material. AM microstructure models can take reference from welding simulations which are relatively more developed [63, 64].

Three models have been used to simulate microstructure for both welding and AM: kinetic Monte Carlo (MC), cellular automata (CA) and phase field modelling (PFM). As mentioned above, microstructure models often fall to two length scales, meso scale and micro scale. In the context of microstructure model, meso scale models tend to model the grain structure of a crystal structure, with little to no data on the microstructure within a grain. Micro scale models on the other hand tend to be deeper in details looking at single or multiple dendrites, sometimes such micro scale models are simulated over a large volume allowing the formation grain structure to found as well. However, such a large model would be computationally expensive and may not be practical or possible for some institutions and companies to replicate [16]. Generally, most MC and CA models fall in the meso scale and PFM in the micro scale.

As microstructure models require a thermal input, they have to be coupled with a thermal model be it using FEM or CFD. The thermal and microstructure model can be weakly coupled and strongly coupled. Weakly coupled simulations can be done sequentially as the microstructure does

not feedback any data back to the thermal model and only the completed thermal simulation data is used for the microstructure model. Strongly coupled simulations require both models to be simulated simultaneously and data transferred and affecting both models, leading to higher accuracies but slower simulation speeds, often one model with higher resolution and/or more equations to solve causing a bottleneck in speed [65]. As such, a weakly coupled model that is simulated sequentially have higher flexibility and may be more practical.

2.3.2.1 Kinetic Monte Carlo Modelling

Kinetic Monte Carlo (MC) modelling is probabilistic by nature and relatively computationally cheap allowing simulations to cover a larger volume making it a suitable meso scale model.

2.3.2.1.1 Kinetic Monte Carlo Modelling Theory

MC models are based on an atomistic simulation, where it has sites regularly placed within in lattice and each site influences the entire system energy. For MC model, each site has an orientation and is compared with its neighbouring sites, if the neighbouring sites have different orientations, this will increase the system energy. The summation of the energy in each site is calculated each step and then each site is given a probability to changing orientation causing a change in the system energy. If the changes cause an increase in system energy, a random number is generated for that site and compared to an acceptance probability, if the randomly generated number is smaller than the acceptance probability this change in orientation is kept, otherwise its orientation remains unchanged. If the change in orientation causes a lower system energy, it is immediately accepted. These are shown in the equations 2.39 and 2.40 [66, 67].

$$\Delta E = J \sum \left[1 - \delta\left(I_j, I_k\right)\right], \tag{2.39}$$

$$P = \begin{cases} exp\,(\frac{-\Delta E}{k_B T_0}), & \Delta E > 0 \\ 1, & \Delta E \leq 0 \end{cases}, \tag{2.40}$$

where ΔE is the overall system energy, J is a scaling factor of the energy system, δ is the Kronecker delta function, lattice assigned number or orientation,I_j, I_k are the number/orientation of the site and neighbour, k_B is the Boltzmann's constant and T_0 is the ambient temperature of the process. Further to the MC simulation, simulating the microstructure requires some modification. Equation 2.40 must be modified to take into account the temperature which affects the possibility to change orientation. The Arrhenius equation is adapted [66, 67]:

$$P = \begin{cases} [M_0 exp\,(\frac{-Q_{act}}{R_{gas}T})] exp\,(\frac{-\Delta E}{k_B T_0}), & \Delta E > 0 \\ M_0 exp\,(\frac{-Q_{act}}{R_{gas}T}), & \Delta E \leq 0 \end{cases}, \tag{2.41}$$

where M_0 is the Arrhenius pre-exponential factor, Q_{act} is the activation energy, R_{gas} is the gas constant and T is the site temperature. While the site may have an assigned orientation, it does not equate to grain orientation but is just an arbitrary number, therefore the model can only predict the size and aspect ratio of the grains. The relatively simple equations to solve means faster simulation speeds allowing larger volume in 3D [68]. Larger volume simulations can take into account multiple tracks and layers [66].

2.3.2.1.2 Kinetic Monte Carlo in Additive Manufacturing

Simulating grain structure using MC method is not new and had been used for casting, sinter and welding. In addition to solidification, other microstructure related changes like recrystallization and grain growth have been predicted using [69, 70]. Welding often cause grain growth in the base material at the heat affected zone (HAZ), Mishra and DebRoy used MC to predict grain sizes in the HAZ in welding of Ti6Al4V [71, 72]. This can be particularly useful for predicting grain

sizes on the base material when using DED for repair. Coupling thermal models to MC for welding showed similarities for adopting to PBF processes [67, 73]. Rodgers *et al.* simulated using MC for electron beam welding and expanded to scanning of multiple track for EBM process [66, 74]. There were some discrepancies between the predicted grain size and aspect ratio but correctly predicted the growth bias towards the scanning direction. MC have shown to be able to get a good grasp of the trend of the grain structure but lack accuracy and details. Literature using MC also showed the possibility of simulating for multiple tracks and layers.

2.3.2.2 Cellular Automata Modelling

Cellular automata (CA) modelling is both probabilistic and deterministic. Grain growth of deterministic while nucleation of seed is probabilistic. CA tends to be relatively more computational expensive as compared to MC but providing more details like grain angles which can be compared against electron backscatter diffraction (EBSD) images from experiment. CA also often simulated in the meso scale.

2.3.2.2.1 Cellular Automata Modelling Theory

CA uses a mesh of cells and each cell have an array of properties. Some of the properties of the cell are the solid fraction, Euler angle, growth length and grain number. The solid fraction is from 0 to 1 where either one is solid or liquid and in between is mushy where it is captured and growing but not solid yet. The Euler angle is the crystallographic orientation at which a cubic structured metal preferential growth angle is in respect to the positive x, y and z axis. The cells are captured when one of the surrounding cell's growth intersects the said cell. The captured cell would copy the grain number and Euler angle. The growth is dependent on the undercooling temperature and found using solidification theory, making the grain growth portion deterministic. The nucleation

of seeds follows a probabilistic approach dependent on the undercooling temperature, ΔT, and the continuous grain density, n [75]:

$$n(\Delta \mathrm{T}) = \int_0^{\Delta T} \frac{dn}{d(\Delta T)} d(\Delta T) \, . \tag{2.42}$$

A Gaussian distribution can be used to determine if a cell forms a nucleus:

$$\frac{dn}{d(\Delta T)} = \frac{n_{max}}{\sqrt{2\pi}} \exp\left[-\frac{(\Delta T - \Delta T_{mean})^2}{2\Delta T_\sigma}\right], \tag{2.43}$$

where n_{max} is the maximum nucleation density, ΔT_{mean} is the mean undercooling when nucleation occurs and ΔT_σ is the standard deviation of the undercooling when nucleation occurs.

2.3.2.2.2 Cellular Automata in Additive Manufacturing

CA have been used extensively for casting and have been extended to predict grain structures in welding and laser cladding processes [76-79]. Wang *et al.* coupled FEM and CA (CAFE) to explore varying laser pulses for laser cladding of Ti6Al4V and its effect on grain structure and its relation to melt pool depth [79]. Another CAFE model simulated a secondary continuous laser behind a primary continuous laser to change the thermal gradient causing the grains to change from columnar to equiaxed grains [80].

Simulated SLM process would differ slightly from the models mentioned above as in both cases such as there is no powder layer or additional material added and different laser profile. But it is still very similar and have been adapted for SLM processes. FDM coupled with CA was used to simulate the grain structure for SLM process in both 2D and 3D [40, 81]. The predicted grain width and aspect ratio were similar with experimental results but there were stray grains in the experimental data that's missing from the simulation results. Lopez-Botello *et al.* added a nucleation function that create a possibility of nucleating new seeds when certain grain size

condition is met [82]. This may help elevate the issue seen in other models that only show columnar grains with no stray grains, though this method would require experimental data first to be able to estimate the grain size condition. CA have also been coupled with CFD and shows grains growing along the simulated melt track geometry, leading to possibly more accurate grain size and aspect ratio [52, 60]. When CA coupled with CFD is that when using Lattice Boltzmann the model is in 2D but managed to simulate multiple tracks, and when using FVM only a single track is simulated.

2.3.2.3 Phase Field Modelling

Phase field modelling (PFM) can simulate from micro to meso scale in terms of microstructure evolution. Most PFM models simulate into great details in the micro scale investigating microstructure changes like grain coarsening, dendrite shapes, solution concentration around the dendrites and dendrite growth in varying conditions [83-85]. PFM is able simulate multiple phenomena to great accuracy but the computational resources required is high and the level of detail and simulation time have to be balanced [86].

2.3.2.3.1 Phase Field Modelling Theory

In MC and CA, the solid-liquid interface is binary while in PFM the interface is diffused and is a fraction across the interface. This allows all variables to be continuous from solid to liquid, not requiring different solutions or rules in each region. However, this interface is very thin and therefore calculation through this interface require very high resolution leading to more computational resources required. The phase field variable, ϕ, range from 0 to 1, where 0 or 1 can be the solid or liquid and vice versa. Simulating the solidification process using PFM, solves for a lower free energy within a system of a certain volume [87-89]:

$$F = \int [f(\phi, c, T) + \omega g(\phi) + \epsilon^2 |\nabla \phi^2|] dV \,, \tag{2.44}$$

where F is the total free energy of the system, f is the thermodynamic potential, c is the concentration, $\omega g(\phi)$ is the double well potential, $\epsilon^2|\nabla\phi^2|$ is the phase field gradient energy and V is the volume. The solid-liquid interface moves as the temperature drops and solidify, making the problem a transient one. To solve this, the Allen-Cahn and Cahn-Hilliard equations can be used [87, 88, 90]:

$$\frac{\partial\phi}{\partial t} = -M_\phi\left[\frac{\partial f}{\partial\phi} + \omega g'(\phi) - \epsilon^2\nabla^2\phi\right], \tag{2.45}$$

$$\frac{\partial c}{\partial t} = \nabla M_c \nabla\frac{\partial f}{\partial c}, \tag{2.46}$$

where M_ϕ and M_c are the motilities of the phase field and concentration field at the interface respectively.

PFM can be extended to solve for multiple phases, for example simulating different allotropic forms of iron in steels, the phases can be expressed as $\phi_i(\vec{x}, t)$ where i denotes the state that the field is. The sum of the phases in a multiphase system has to reach unity, $\sum_{i=1}^{N}\phi_i = 1$ [88].

2.3.2.3.2 Phase Field Modelling in Additive Manufacturing

PFM have also been used to simulate solidification in casting and welding, getting the solute concentration, nucleation and dendrite arm spacings [91, 92]. Similar properties were simulated for the EBM process, where 2D/3D FEM models provided the data on temperature and thermal gradients and coupling to 2D PFM [93-95]. The PFM models uses a smaller geometry as compared to the thermal model and simulate a portion of the time where the heat source passes through. The PFM model also have seeds at fixed locations which grows when the liquid changes to solid and

the distance were usually found from prior experimental data. The distance apart can affect how long the primary or secondary dendrite arms grow as well as the solute concentration between the dendrites. The flow within the melt pool can influence the dendrite growth, Acharya *et al.* strongly coupled CFD and PFM and found dendrites grew faster towards the surface when the scanning speed was slower while faster scanning speed lead to dendrites growing faster towards the scanning direction [96, 97].

2.3.3 Comparison of Modelling Methods

Choosing the appropriate simulation model depends largely on the computational resources available, input and output requirements. CFD and PFM provide the ability to simulate to higher accuracies, however, using both would also mean requiring large computational resources, often requiring high performance computing to complete simulating within a practical time frame. Simulating more than a single track for either CFD and PFM may pose a challenge and when investigating situations that require more than a single track may not be able to use these two models. Finding the thermal profile of different scanning strategy, investigating the thermal effect over multiple layers are some examples that would require simulating more than a single track. In such cases FEM and MC or CA may make better choices. Both have been shown to be able to simulate multiple tracks and even layers in 3D. In terms of output, MC lack information on the grain angles but still be able to capture the trend and shape. CA on the other hand is deterministic and may provide more accuracies when simulating varying process parameters. The comparison between the models is summarized in Table 2-1.

Table 2-1 Comparison of capabilities between microstructure models: kinetic Monte Carlo, cellular automata and phase field modelling.

Simulation method	Kinetic Monte Carlo	Cellular Automata	Phase Field Modelling
Multiple grains level	✓	✓	×
Sub grain level	×	×	✓
Multiple build layers	✓	✓	×
3D profile	✓	✓	×
Experiment for tuning	✓	×	×
Probabilistic	✓	✓	✓
Deterministic	×	✓	✓
Commercial software	×	×	✓
References	[66, 67, 69-74, 98]	[40, 52, 60, 77, 79-82, 99, 100]	[53, 85, 91-96, 101]

2.3.4 Validation and Comparison of Simulation Models Against Experimental Results

While some literature does not validate simulation against experimental results, it is helpful to compare the simulation results to experiment data as this provides a reference on the models' results and how the assumptions hold against experimental results. What properties and dimensions are compared depends largely on the simulation models goals. FEM and CFD simulating the thermal reaction from energy input on the material usually compares the melt pool width and depth based on micro-segregation seen in etched samples under optical microscopy and scanning electron microscope (SEM) [41, 102]. The difference between melt pool width and depth found in simulation compared to experiment ranges from 5 to 30% [41, 43, 44, 102]. Another method used to validate FEM simulations is to measure the temperature of the substrate near the

melt pool, however, this set up cannot validate the melt pool characteristics and also require more specialized set up experimentally [103].

Comparison of microstructure depends largely on the scale of the simulation. MC and CA methods usually simulate the grain structure and the grain shape is compared using SEM and electron backscatter diffraction (EBSD), in addition as CA can simulate the grain angles, some compare the frequency of high angle and low angle grain boundary [80, 104, 105]. PFM models usually simulate the dendritic growth and SEM is used to compare the dendrite growth shape and primary dendrite arm spacing [53, 95, 96].

2.4 Research Gap

Most literature do not explore the effects of scanning strategy effect on the thermal gradient and grain structure. Models that simulated multiple layers did a single line scan per layer. Exploring different scanning strategies can be useful as shown that changing from continuous scanning to spot scanning can change the grain structure from columnar to equiaxed grains [106, 107]. This research explore the use of FEM and CA to be able to simulate multiple process parameters, including scanning strategy, for multiple layers. FEM and CA were chosen because literature show they are the most practical to simulate for large volumes while keeping the simulation based on physics.

FEM and CA models shown in literature do not always fully show how the CA model is created and thus is not known if the model can accommodate simulating for larger volumes that is required for simulating different scanning strategies. This research would show how the model is created,

programming language used and the parallelisation method using MATLAB to ensure the model can simulate larger 3D models within a more practical time range.

Chapter 3 Methodology

Simulating grain structure needs a thermal model in order to get the temperature profile of the laser on the base material and coupling it to a microstructure model. This research used FEM for the thermal model and CA for the microstructure. This chapter documents the methodology of FEM, CA and experiment done on SS 316L. This research simulated both SS 316L and Ti34Nb. The experimental results for Ti34Nb would be referenced from Huang *et. al.* [108].

Cellular automata – finite element method (CAFE) takes the temperature history from the FEM model and interpolates it to CA model to simulate the microstructure. FEM and CA uses mesh for simulation, FEM typically uses a much larger element size as compared to CA. As such the typical CAFE model would have two different meshes, a larger one for FEM and another with much smaller element size for CA. Due to the different element sizes, FEM would use a larger time step compared to CA. Thus, for each FEM time step, there would be multiple CA time steps. The temperature in the FEM mesh has to be interpolated to the CA mesh for each FEM time step. CA calculations would then run to get the microstructure to match the FEM time step. The calculation loops on to the next FEM time step till all the FEM time steps are completed. The computation steps are shown in Figure 3-1. This research would look at sequentially coupled CAFE as it provides flexibility in solving the FEM and CA separately while using less computational resources and time.

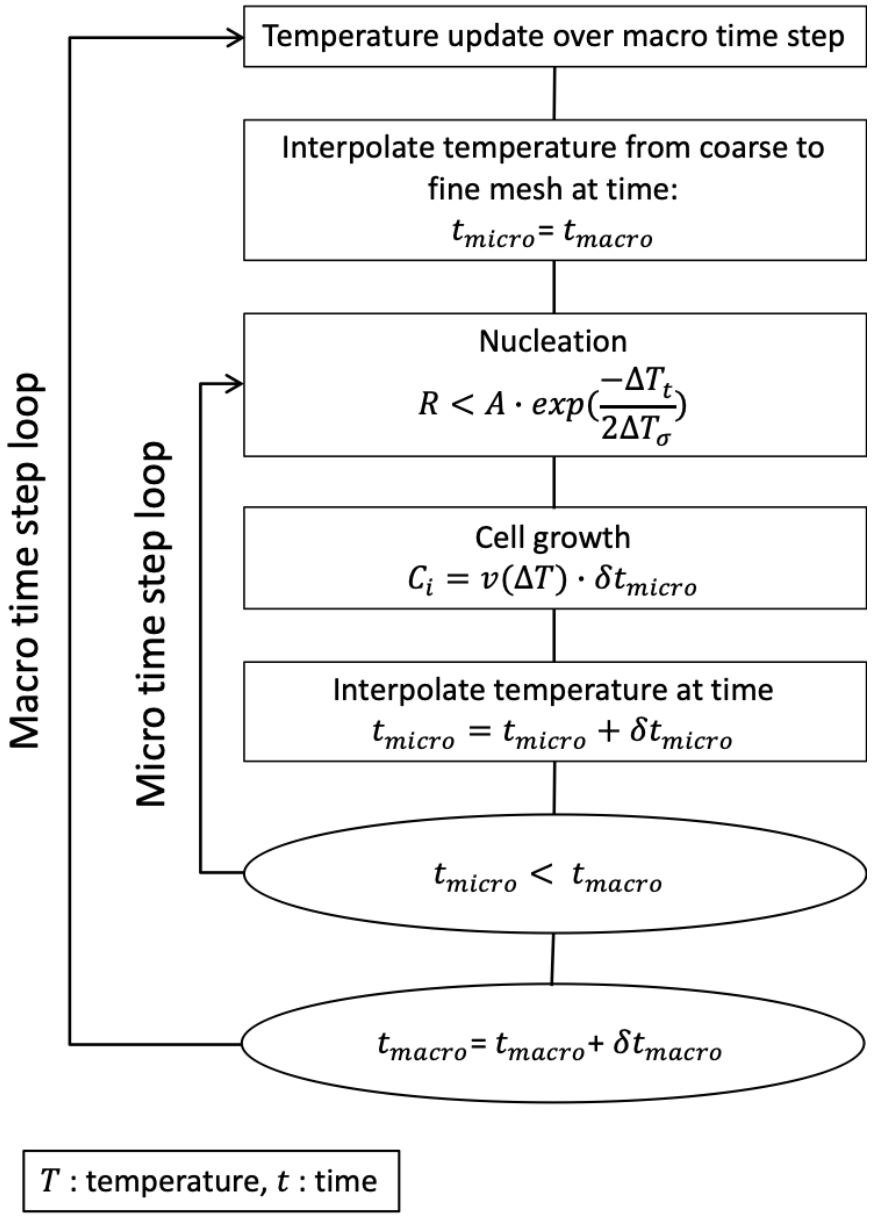

Figure 3-1 Sequentially coupled cellular automata-finite element loop.

3.1 Finite Element Method

This research uses FEM to solve the non-linear transient thermal problem of the SLM process and FEM software COMSOL Multiphysics (COMSOL Inc., Sweden) was used. FEM solves the laser-powder interaction to find the temperature of the powder and substrate during the SLM process [41, 48]. The thermal conductivity of powders and substrate was solved by the PDE in equation

3.1. The loss of heat by convection and radiation are considered as boundary conditions to the PDE (equations 3.2 and 3.3).

$$\rho c_p \frac{\partial T}{\partial t} - \nabla \cdot (K \nabla T) = Q, \tag{3.1}$$

$$q_{conv} = h(T - T_0), \tag{3.2}$$

$$q_{rad} = \sigma \varepsilon (T^4 - T_0^4), \tag{3.3}$$

where ρ is the density, c_p is the specific heat capacity, K is the heat conductivity, h is the coefficient of heat convection, σ is the Stefan-Boltzmann constant, ε is the emissivity, T_0 is the ambient temperature, Q is the heat input. The convection and radiation are accounted for on the top surface as a boundary condition. The heat input is a laser beam and its distribution can be a top-hat profile or Gaussian profile [41]:

$$Q_{top-hat} = \frac{2AP}{\pi r_0^2} \exp\left(-\frac{2(x^2 - y^2)^5}{r_0^{10}}\right)), \tag{3.4}$$

$$Q_{Gaussian} = \frac{2AP}{\pi r_0^2} \exp\left(-\frac{2(x^2 - y^2)^2}{r_0^2}\right)), \tag{3.5}$$

where A is the absorptivity of laser, P is the laser power and r_0 is the laser beam radius. The powder and substrate experience phase change when heating from solid to liquid and vice versa, the latent heat of fusion is considered in the specific heat capacity. The specific heat capacity change from solid properties to liquid properties by the following equations:

$$c_p = \frac{1}{\rho}\left[\theta \rho_s C_{p,s} + (1 - \theta)\rho_l c_{p,l} + \Delta H \frac{\delta}{\delta T}\left(\frac{(1 - \theta)\rho_l - \theta \rho_s}{2[\theta \rho_s + (1 - \theta)\rho_l]}\right)\right], \tag{3.6}$$

where ρ is the density of solid or liquid, c_p is the heat capacity of solid or liquid, θ is the phase fraction from zero to one and ΔH is the latent heat of fusion.

The model has elements of two materials, powder and substrate. At temperatures above the liquidus temperature, the powder and substrate have the same properties. While at temperatures lower than the solidus temperature, the powder properties are a fraction of the substrate according to the porosity.

$$K_{powder} = K_{substrate}(1 - \emptyset)^{x} \,, \tag{3.7}$$

$$\rho = \rho_{substrate}(1 - \emptyset) \,, \tag{3.8}$$

where $\emptyset$ is the porosity and x is the scaling factor with a value of 0.4 [41]. After the powder elements changes phase from solid to liquid, upon cooling, it solidifies to solid substrate material instead. In order to account for the Marangoni effect, the thermal conductivity was artificially increased for temperatures above the liquidus temperature [109]. This study simulated for SS 316L and Ti34Nb. The scanning strategy for both materials uses a combined track, where short single line scans moving in a certain direction which can cause a large melt pool to form, this is shown in Figure 3-10. A larger melt pool can potentially be more stable and have a different thermal gradient.

3.1.1 Stainless Steel 316L

The time taken for a single combined track to complete 10 mm of distance or more would allow the start of the combined track to cool significantly, moreover, the CA model would take significantly long to simulate 10mm of track. As such the FEM model simulate 3mm of distance for a combined track, cooling for the duration taken for the rest of the 7mm combined track before heating the next combined track. In total three combined tracks were simulated in the FEM model. The material properties and parameters are shown in Figure 3-2, Figure 3-3 and Table 3-1.

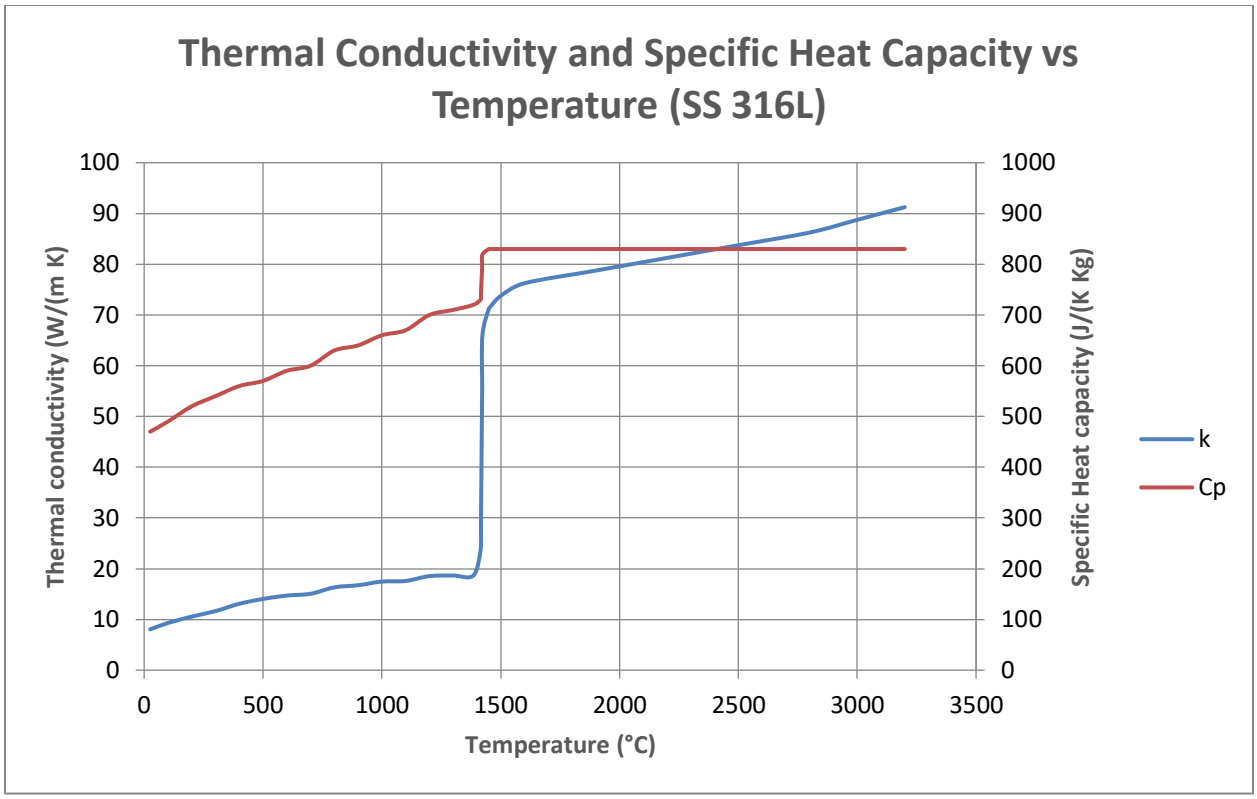

Figure 3-2 Thermal conductivity and specific heat capacity of SS 316L used in finite element simulation [110].

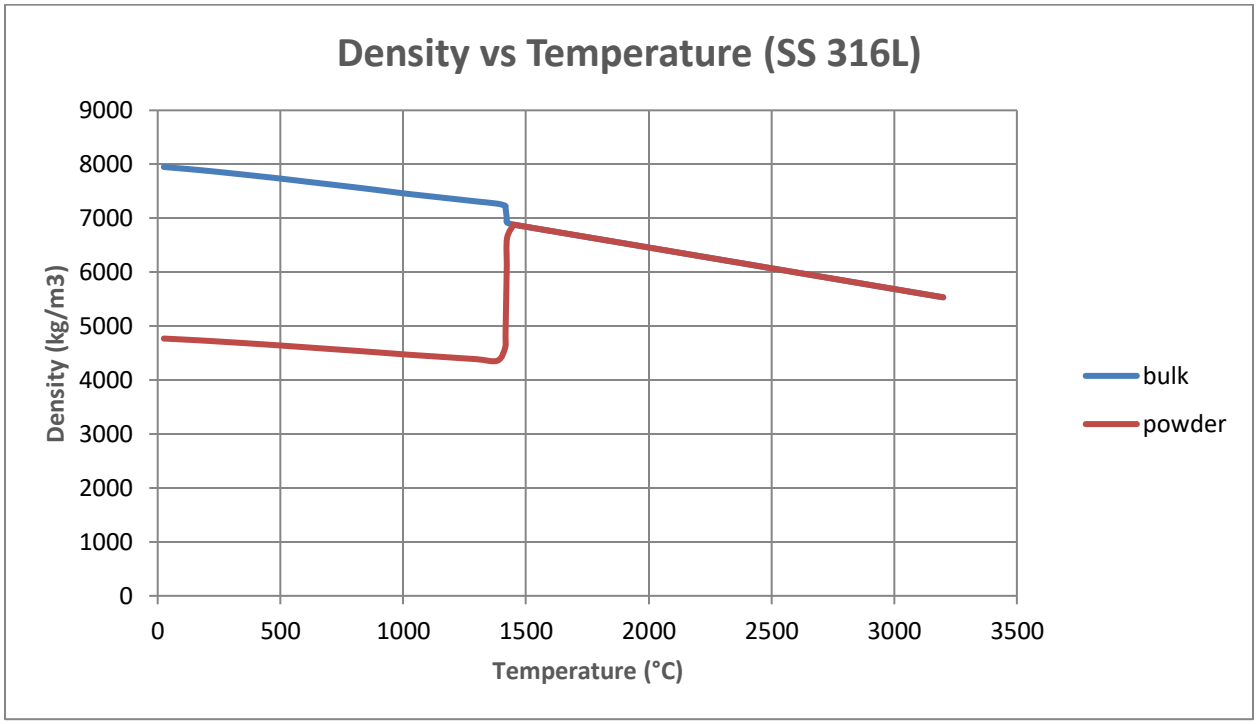

Figure 3-3 Density of SS 316L used in finite element simulation [110].

Table 3-1 Parameters used for SS 316L in finite element simulation.

Parameter	Symbol	Value	References
Laser radius (top-hat)	r_0	100 μm	
Emissivity	ε	0.22	[111]
Absorptivity	A	0.8	
Ambient temperature	T_0	293.15 K	
Latent heat of fusion	ΔH	285000 J/Kg	[110]

3.1.2 Ti34Nb

Simulating the thermal model for Ti34Nb is similar to the SS316L thermal model, however, instead of three combined tracks, only a single combined track is simulated and two different power and laser profiles were used. A lower power of 350 W and Gaussian profile and a higher power of 950 W and top-hat profile were simulated. The properties and parameters are shown in Figure 3-4, Figure 3-5 and Table 3-2.

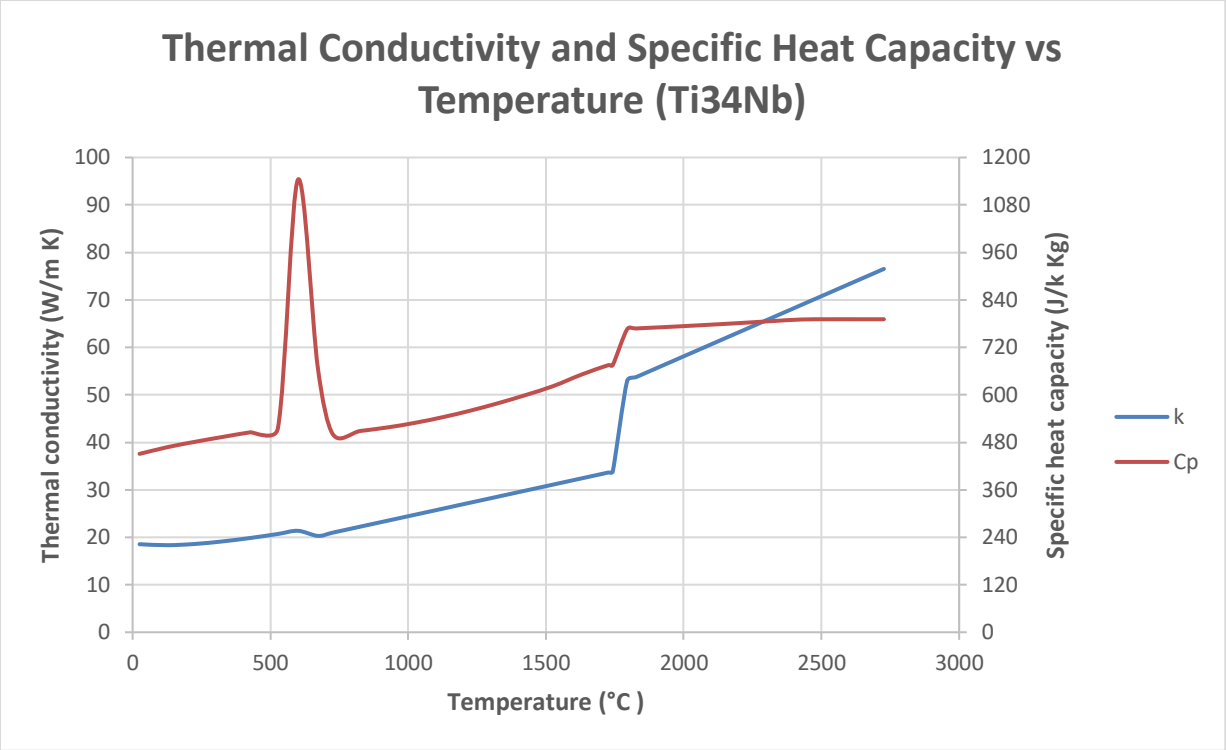

Figure 3-4 Thermal conductivity and specific heat capacity of Ti34Nb used in finite element simulation.

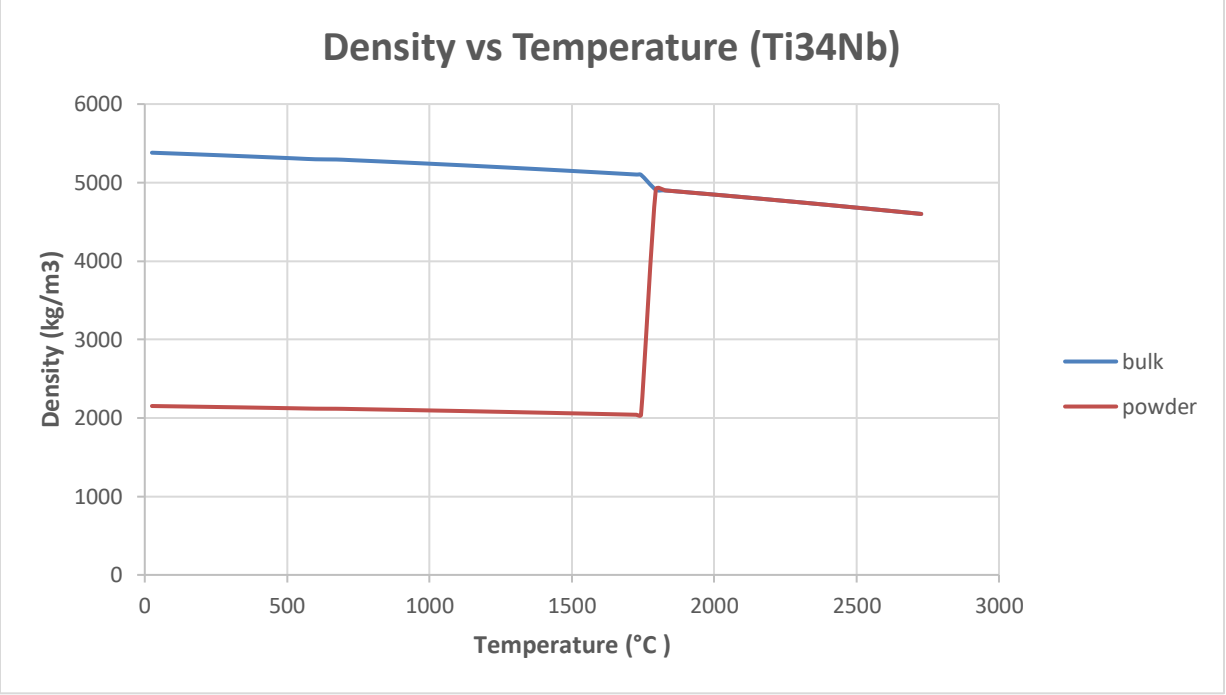

Figure 3-5 Density of Ti34Nb used in finite element simulation.

Table 3-2 Parameters used for Ti34Nb in finite element simulation.

Parameter	Symbol	Value	References
Laser radius (top-hat)	r_0	100 µm	
Laser radius (Gaussian)	r_0	40 µm	
Emissivity	ε	0.22	[111]
Absorptivity	A	0.15	
Ambient temperature	T_0	293.15 K	
Latent heat of fusion	ΔH	293261 J/Kg	

3.2 Cellular Automata Modelling

Simulating for CA usually uses square cells for 2D and cubic cells for 3D. The state of each cell is dependent on neighbouring cells as well as transitioning due to other rules. The neighbouring cells can be of two types: Von Neumann and Moore neighbourhood (Figure 3-6) [76, 112]. Von Neumann neighbourhood only has the adjacent cells like a diamond shape as neighbours giving 4 neighbours in 2D and 6 neighbours in 3D. Moore neighbourhood takes a square around the cell as neighbours leading to 8 neighbours in 2D and 24 in 3D. This study uses the Moore neighbourhood method.

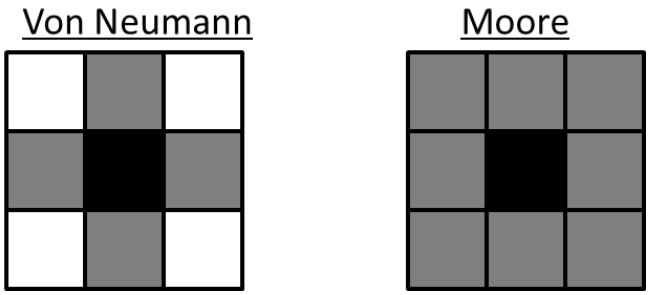

Figure 3-6 Different neighbourhood patterns in CA, grey cells are the neighbours of black cell.

Transiting the state of cells is dependent on solidification theory which determines two conditions:

1. Nucleation of liquid cells
2. Dendritic growth of solid cells

Every cell that has its temperature above the solidus temperature would be considered liquid and assigned a random number between 0 and 1. The nucleation density is calculated every time step using equation 3.9. The distribution of nucleation is taken to be Gaussian and the nucleation around the melt pool wall and the bulk liquid is taken to be different. The number of new nucleation site can be found as such:

$$N_w = \frac{n_{w,max}}{\sqrt{2\pi}} \exp\left[-\frac{\left(\Delta T - \Delta T_{w,mean}\right)^2}{2\Delta T_{w,\sigma}}\right] N_{aw}, \tag{3.9}$$

$$N_b = \frac{n_{b,max}}{\sqrt{2\pi}} \exp\left[-\frac{\left(\Delta T - \Delta T_{b,mean}\right)^2}{2\Delta T_{b,\sigma}}\right] N_{ab}, \tag{3.10}$$

where N_w and N_b is the number of nucleation sites in the melt pool wall and bulk liquid respectively, N_{aw} and N_{ab} is the total number of cells at the melt pool wall and bulk liquid respectively. Each time step, the ratio of the number of nucleation and the total number of cells (i.e. N_b/N_{ab}) and compared the the randomly assigned number. If the number is less than the ratio, the cell is considered a nucleation site and the cell changes from liquid to solid. As it changes state, the cell is also assigned a random crystallographic direction.

Cells can also convert from liquid to solid by being captured by other growing solid cells. This is to simulate the dendritic growth. The velocity of the dendrite growth is calculated every time step with higher weighting to the preferential growth direction. The velocity of the dendrite growth is calculated by solidification theory models like the KGT method.

A 3D CA model was developed using MATLAB. The temperature found using FEM was used as input for the CA model. As the mesh of the CA model is finer than that of the FEM model, the temperature has to be interpolated to the CA cells. The temperature of each cell is interpolated from the closest four nodes from the FEM mesh.

3.2.1 Stainless Steel 316L

The CA model is first initialized by growing random seeds to the average width of 10 µm. The seeded grains have a random orientation between 0° to 360° in x, y and z axis. Three combined tracks were simulated for each layer and two layers were simulated (Figure 3-7). The tracks were also rotated 90° for the second layer. The values used for CA were calculated using the KGT method and the parameters given in Table 3-3. The velocity of dendrite growth against the undercooling temperature can be found (Figure 3-8), thus having each CA cell grow according to its undercooling temperature found from the FEM model.

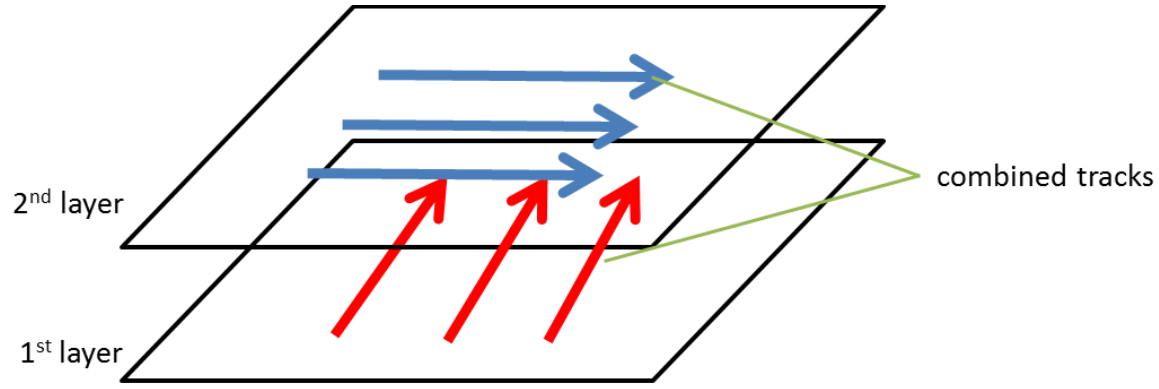

Figure 3-7 Representation of the simulated tracks, where three combined tracks are simulated for each layer and rotated 90° in the second layer. Red arrows are tracks in the first layer and blue arrows are tracks in the second layer.

Table 3-3 Parameters used for cellular automata simulation of SS 316L

Parameter	Symbol	Value	References
Diffusion coefficient in liquid	D^l	$1.8 \times 10^{-9} m^2/s$	[113]
Gibbs-Thomson coefficient	Γ	$3.0 \times 10^{-7} Km$	
Liquidus slope	m^l	$-2K/wt\%$	
Partition coefficient	k	0.9	
Initial concentration	C_0	$17.0wt\%$	
Maximum nucleation density	$n_{b,max}$	$7 \times 10^8 m^{-3}$	[81]
Mean undercooling temperature	$\Delta T_{b,mean}$	$2.5K$	
Standard deviation of undercooling temperature	$\Delta T_{b,\sigma}$	$1.0K$	

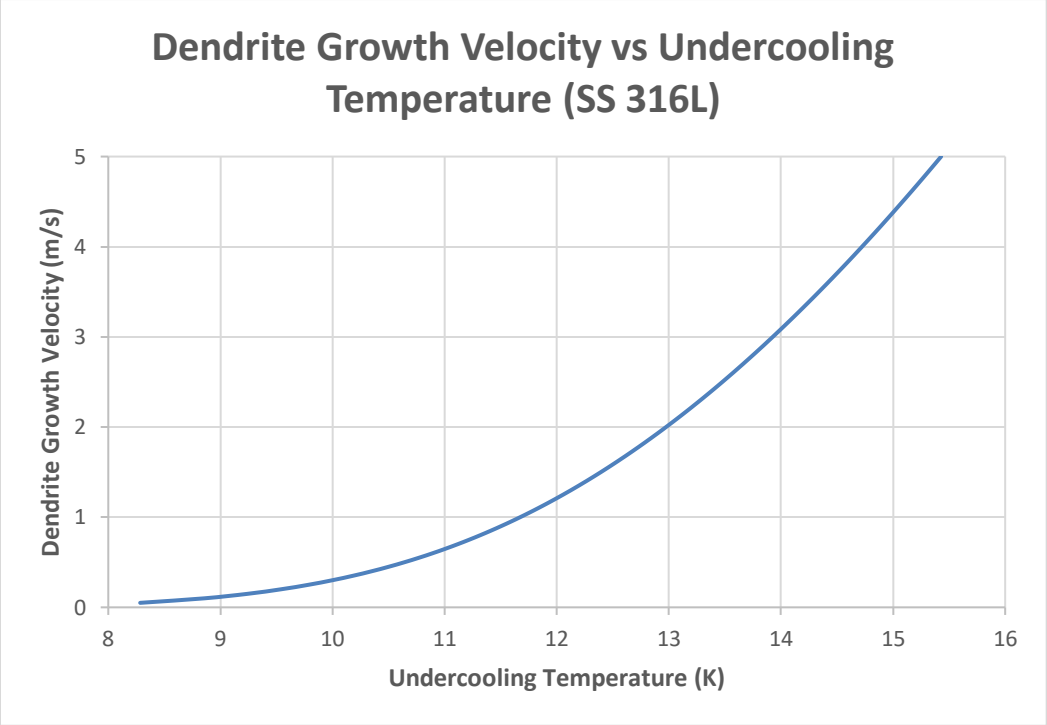

Figure 3-8 Plot of the dendrite growth velocity against undercooling temperature of SS 316L

3.2.2 Ti34Nb

Simulating Ti34Nb on the experiment done by Huang *et. al.* for two different power, 350 W and 950 W. For the 350 W power, a single combined track was simulated while for the 950 W power, three combined tracks were simulated for a single layer. The reason for this is because the resultant melt pool for the 350 W power was small and lead to a single combined track to have simulated multiple track lines, while the 950 W resultant melt pool was large leading to only a single track. The resultant grain size would be compared against the experimental data. The CA model was first initialized with grain width average 10 μm, and seeds were random in the x and z axis but limited from 0° to 25° and 335° to 360° in the y axis, where the y axis is the building direction. The reason being that titanium-niobium alloys produced by SLM seem to have most grains growing in the <100> direction and as such have the initial seeds close to this direction [114, 115]. The parameters and the velocity of dendrite growth against the undercooling temperature can be found in Table 3-4 and Figure 3-9 respectively.

Table 3-4 Parameters used for cellular automata simulation of Ti34Nb.

Parameter	Symbol	Value	References
Diffusion coefficient in liquid	D^l	$7.33 \times 10^{-8} m^2/s$	[53]
Gibbs-Thomson coefficient	Γ	$1.94 \times 10^{-7} Km$	
Liquidus slope	m^l	$6\ K/wt\%$	
Partition coefficient	k	1.25	
Initial concentration	C_0	$34.0 wt\%$	
Maximum nucleation density	$n_{b,max}$	$7 \times 10^8 m^{-3}$	[81]
Mean undercooling temperature	$\Delta T_{b,mean}$	$2.5K$	

Standard deviation of undercooling temperature	$\Delta T_{b,\sigma}$	$1.0K$	

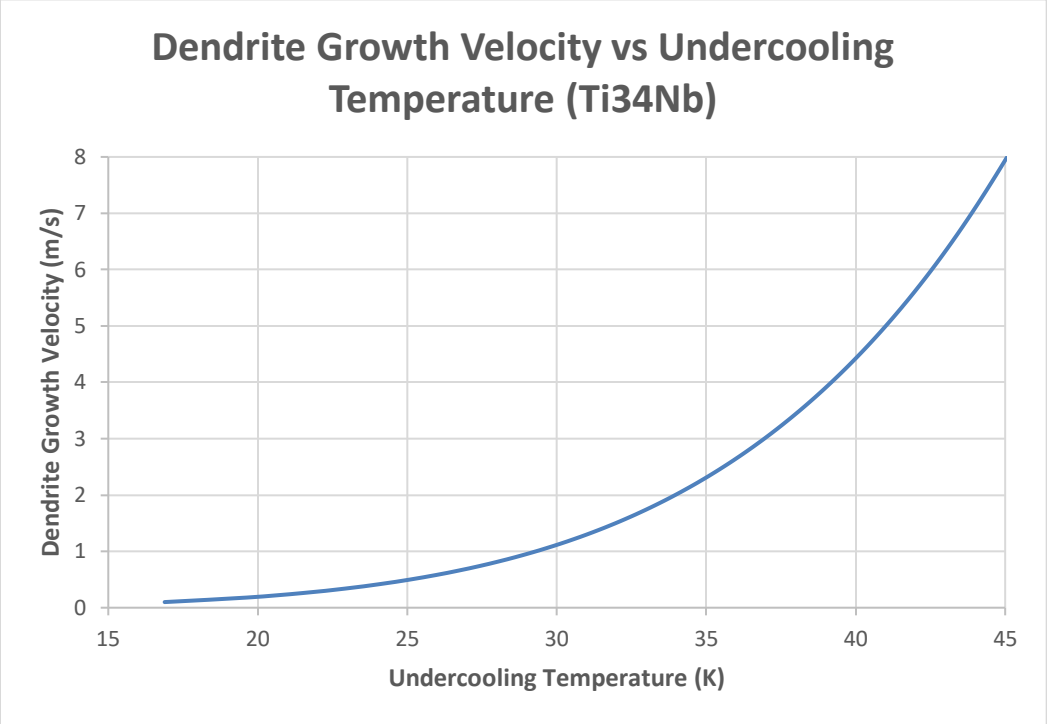

Figure 3-9 Plot of dendrite growth velocity against undercooling temperature of Ti34Nb.

3.2.3 Conversion of Euler Angles to IPS Colouring

The Euler angles simulated in the CA model does not produce the colour scheme commonly used in electron backscatter direction (EBSD) which is inverse pole figure (IPF)-colouring. IPF-colouring is commonly used to show the crystal direction relative to a certain sample direction quickly using colours. DREAM.3D was used in order to convert Euler angles to IPF-colouring [116]. The following pipeline in DREAM.3D was used to convert Euler angles gotten from the CA model simulated in MATLAB:

Create Data Container
Create Geometry
Import ASCII Data
Create Data Array
Combine Attribute Arrays
Convert Angles to Degrees or Radians
Create Ensemble Info
Generate IPF Colors
Write DREAM.3D Data File

3.3 Experimental Setup

Changing laser power and scanning speed affects print quality and production time. Using high power and fast speeds lead to discontinuous tracks [117]. To create a stable long track, a different scanning pattern is proposed. The scanning strategy consists of a meandering pattern of short width (500 μm). The meandering pattern is accounted as a single track and would be referred to as a "combined track: (Figure 3-10). Due to the shorter scan lines, melt pool of the previous scan is reheated again. This causes the melt pool to expand leading to a large melt pool that slowly moves along the meandering track, thus creating a single large track (termed as combined track). The combined track had a stable melt pool that led to a continuous line with no breakage along the entire width.

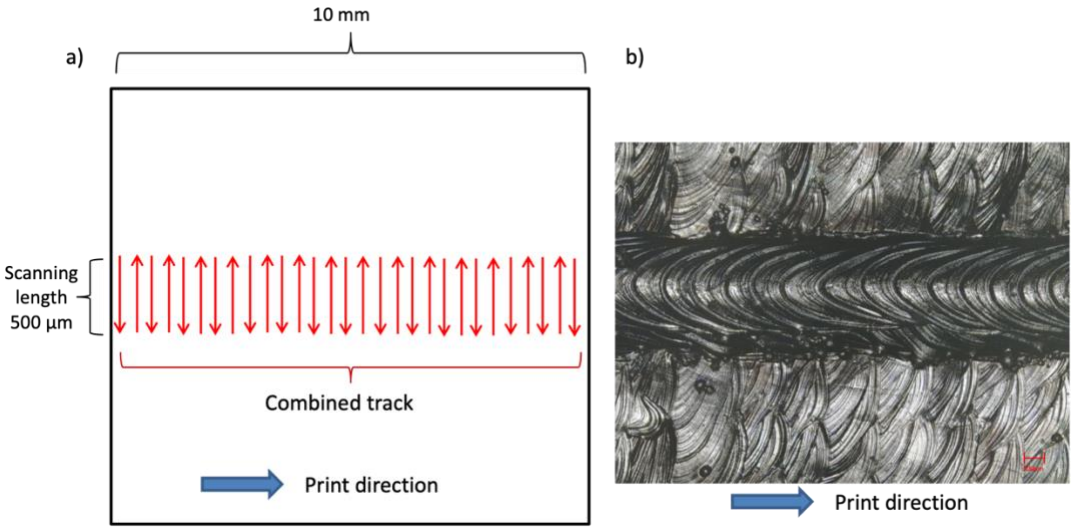

Figure 3-10 a) Schematic representation of the scanning strategy termed as "combined track" which consists of meandering short scans b) Microscope image of the stainless steel part printed using the scanning strategy.

Fabrication of the SS 316L material was carried out using SLM®500 HL (SLM Solutions Group AG, Germany) and three 10 × 10 × 5 mm cubes were fabricated for characterization. The cross sections of the samples were polished using SiC paper followed by MD-Largo and finally polished with MD-Dac. The samples were then etched using Kroll's reagent (1–3% HF, 2–6% HNO_3 and 91–97% H_2O) and inspected by optical microscope (OM; ZEISS Axioskop 2 MAT). The process parameters used were a laser power of 950 W, scanning speed of 1.95 m/s and hatch spacing of 62.5 µm. Melt pool depth, width and grain size are characterize from the cross sections of the samples.

This research would analyse SLM of Ti34Nb with similar scanning pattern. Two cases were simulated and compared against the experiments [108]. The first case has the laser power of 950 W and 1.00 m/s scanning speed and second case with laser power of 350 W and 0.35 m/s scanning speed keeping the energy density constant in both cases.

Chapter 4 Results and Discussion

4.1 CA Model

MATLAB was chosen to create the model as it uses simple language and is optimized for fast array functions which CA uses. It is also considerably easier to create parallel program as compared to using C++. While C++ can give more control over computer resources, it also means other issues have to be controlled like memory leaks and garbage collection. MATLAB while it may not be as fast and do not provide as much control on the system, can be easily coded and need not worry about security issues.

The temperature file is loaded and iterate through in macro time steps and CA model runs the micro time steps loop for every macro time step as shown in Figure 3-1. The pseudo-code for each CA micro time step is provided below:

```
Interpolate temperature per micro time step
If (cell temperature > melting temperature)
    Convert all cell angles, growth length, decentered square position and cell fraction to 0
Get volume of melted region
Calculate if possibility of nucleation
If (cell can nucleate)
   Set random cell angles, growth length to 0.1 of cell length, centred decentered square
position
Loop through cells with cell fraction = 0.5 and below melting temperature
   Increase growth length according to the cell undercooling temperature and dendrite growth
theory
Pad all arrays along edges to aid subsequent calculations
Loop through cells checking if growth length has extended to neighbouring cells
If (growth length have extended beyond neighbouring cells)
   If (neighbouring cell have cell fraction = 0)
      Set neighbouring cell angle to the same as current cell angle, the current decentered square
position captured, change cell fraction to 0.5 and set growth length according to the
undercooling temperature and dendrite growth theory
Loop through cells checking if it is surrounded by cells with cell fraction 0.5 or 1
If (cell is surrounded by cell fraction = 0.5 or 1
```

Change cell fraction to 1
End loop

Testing that the code worked as intended was done by using a single seed in the middle with fixed cell angles and two scenarios, one with constant temperature and another with a temperature gradient towards one of the corners. In the first scenario, the seed should grow at a fixed angle evenly through the <100> direction. In the second scenario, the seed should grow more towards the cooler temperature at the fixed angle. This is shown in Figure 4-1.

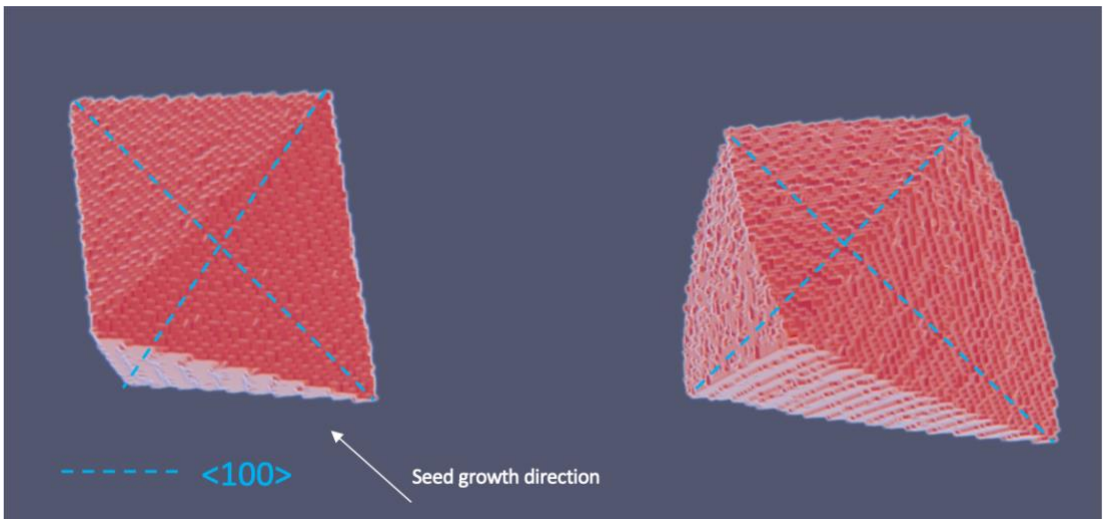

Figure 4-1 On the left a single dendrite grown in constant temperature and on the right a single dendrite grown in a temperature gradient.

Decentered square method was used as it provided more accuracy to the model, capturing cells earlier and is not affected by any mesh bias caused by having cube shape for the cell. Figure 4-2 show the grains being biased and only grow slightly to the side when used without decentered square while the model that used decentered square showed the grains growing sideways according to the cell angles. This allows the model to capture the competitive grain growth seen in experiments.

- Without decentered square

- With decentered square

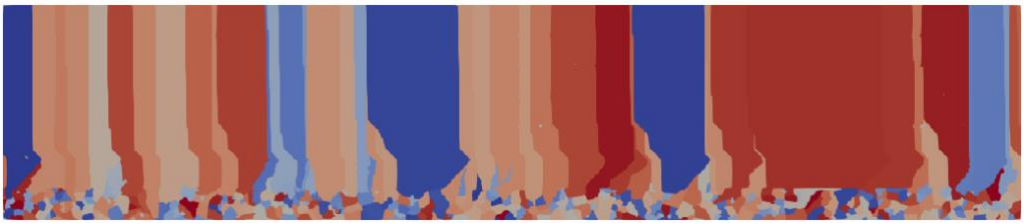

Figure 4-2 Two models showing the difference in using decentered square method.

4.1.1 Parallelization

Parallelization in MATLAB using the function *SPMD* which allows a single program to run with multiple data. Unlike C++, MATLAB does not allow the control of cores or thread that the program runs in but instead run multiple "workers" similar to running multiple MATLAB instances for the same program. Parallelization is helpful when the number of cells is large, like when converting 2D models to 3D models. For a cell size of 1μm, a 2D model of size 2.2 X 0.14 mm would have approximately 308 thousand cells while a 3D model of size 2.2 X 0.14 X 0.2 mm would have approximately 61 million cells. Using a single worker would increase the computing time for 2D to 3D model from minutes to days, even possibly weeks.

Parallelization works by splitting the model into multiple models, this splits the arrays for each "worker" to run the calculations thereby increasing the speed accordingly (Figure 4-3).

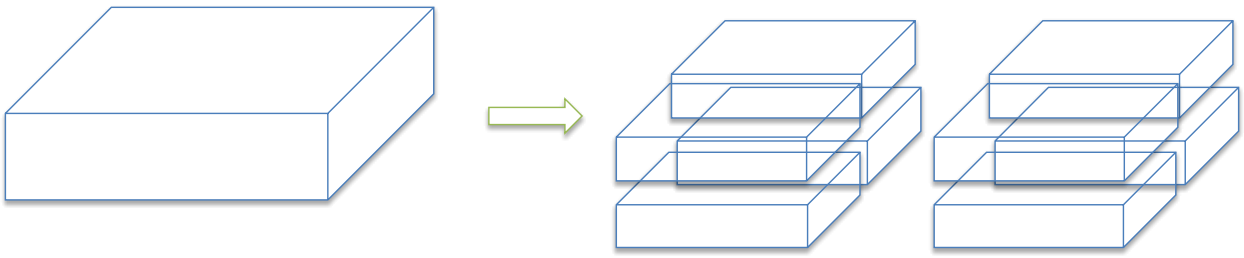

Figure 4-3 Example of array being split for parallelization.

This is not without drawbacks, as the different workers do not share data with each other. Additional steps have to be taken after each micro time step to send the information of the neighbouring edges so that each model have the most up to date information like the cell angles, growth length and cell fraction. This is achieved by first padding the arrays with information from surrounding models and with every micro time step the information is sent between each model and the padded array information is updated, an example is shown in Figure 4-4. This addition brings about additional computing time called overhead and because the more the model is split the more overhead is needed, there is a point in which the model does not receive as much additional benefit from being split further. The efficiency of the model with multiple workers can be calculated using the time taken for a single worker to simulate divided by the product of the time taken for multiple workers to simulate and the number of workers used:

$$\mathrm{E} = \frac{t_{single}}{t_{multiple} n_{multiple}}. \tag{4.1}$$

As shown in Figure 4-5, testing a model that had 30 million cells, simulating it in one worker took 72 hours, this was decreased to 25.2 hours when using 2 workers and 10.6 hours when using 10 workers. However, the efficiency was constantly dropping. The efficiency is dependent on how complex the calculation, size of the model and amount of information is required to transfer and

is most likely to decrease even more as more worker is added. In this case, for the hardware and MATLAB license used, 12 workers were the maximum and may most likely taken the lowest time and thus the maximum number of workers could be used. It should be noted that the model is running using data loaded to the memory which would allow faster reading and writing as compared to loading using the hard disk. Overhead not only uses additional computing time but additional memory. The amount of memory in the hardware should be more than the model requires or the speed will become dependent on the hard disk read and write speed.

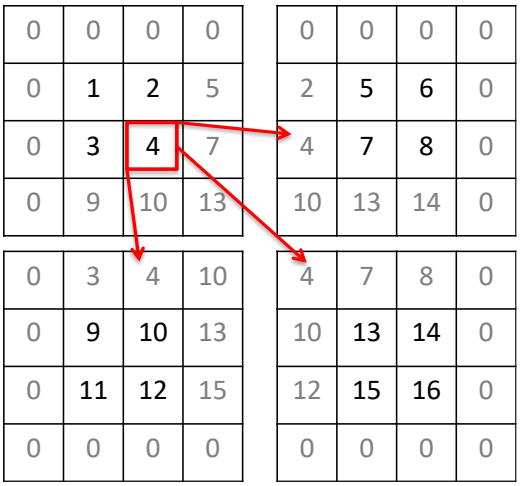

Figure 4-4 Example of arrays being padded and transferring of data to surrounding models.

Workers	1	2	4	8	10
t (hours)	72	25.2	15.8	11.3	10.6
E (%)	-	143%	114%	80%	68%

Figure 4-5 Efficiency of parallel models for a given model.

4.2 Simulation and Experimental Data Comparisons

4.2.1 Stainless Steel 316L

Grain structure of as-built SLM SS 316L parts show epitaxial growth leading to columnar grains in the build direction. The columnar grains grow through multiple layers. Competitive grain

growth occurs within the first few layers with selected grains growing larger and eventually growing beyond multiple layers. The columnar grains show certain patterns, fanning out as it grows through the layers, grow straight up and zigzag across the layers (Figure 4-6). Competitive grain growth also happens across the layers. The grain width varies largely from 100 to 600 µm with a mean of 273 µm and a standard deviation of 138 µm. The grains are relatively coarse compared to process parameters that use single line scans having grain width approximately around 10 to 25 µm [118, 119]. Although the grain width is different, the pattern of the grain structure is similar, where columnar grains predominately grow in the building direction growing through multiple layers.

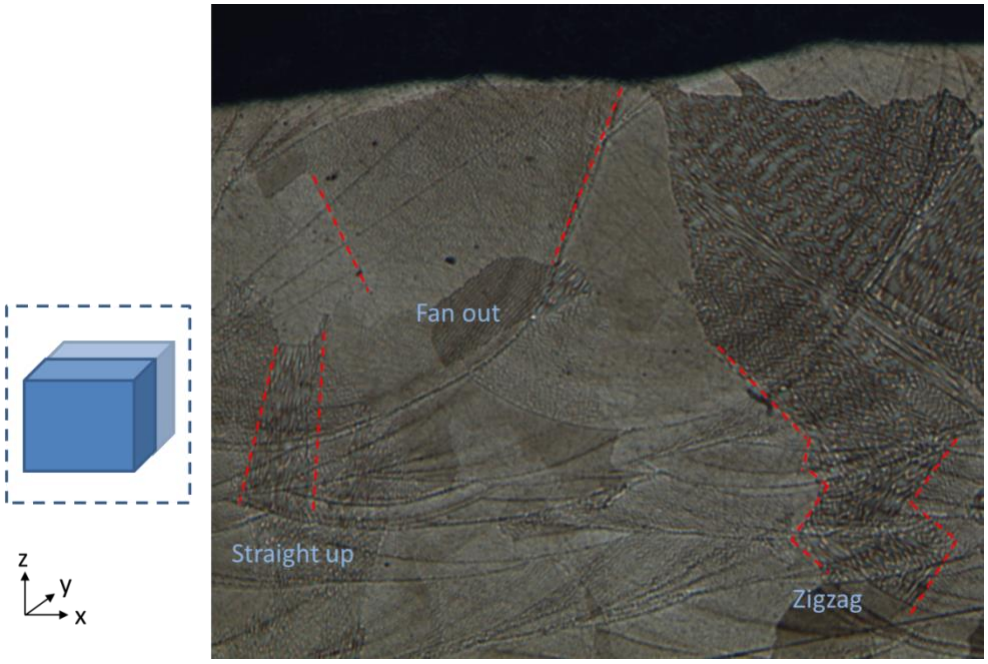

Figure 4-6 Grain patterns seen in selective laser melted SS 316L part. Optical image obtained across the x-z plane of printed cube.

4.2.1.1 Melt Pool Dimensions

The melt pool dimensions were found using FEM simulation and from micrographs of printed samples. The melt pool width was found to have a mean of 883 µm and a standard deviation of 304 µm in the printed samples and 820 µm in the simulation. The melt pool depth was found to

have a mean of 337 µm and a standard deviation of 107 µm in the printed samples and 328 µm in the simulation which is shown in Figure 4-7. The error in width and depth is 7.0% and 4.6% respectively and was considered as acceptable. The width of the pool in the printed sample varies from 700 µm to 1200 µm. A possible reason for this is the built up of heat as well as previously solidified region having different properties as the powder bed. This can be seen in Figure 4-7 where the melt pool does not solidify in a round shape but tapered off at the top causing a larger melt pool width.

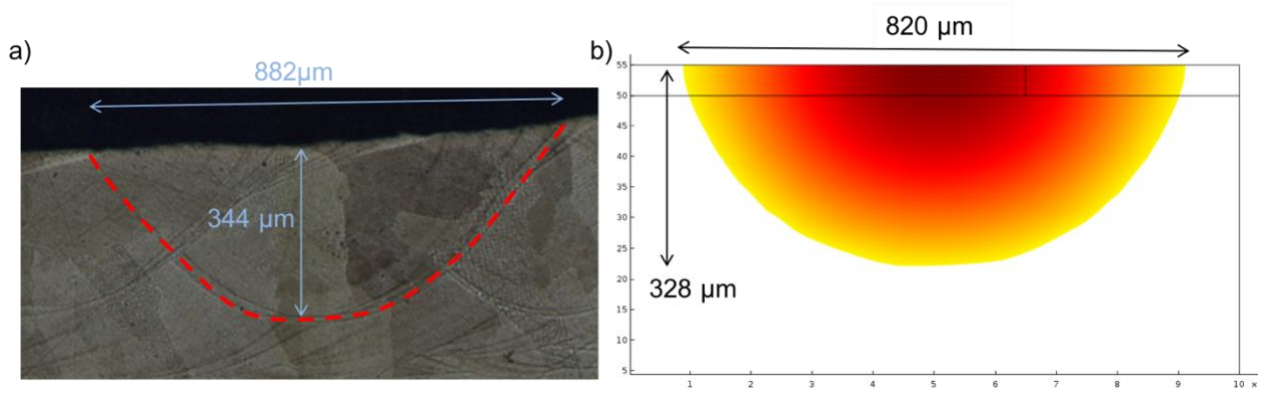

Figure 4-7 Measured melt pool dimensions in a) printed sample and b) FEA simulation.

The melt pool width is larger than the scanning length (500 µm) by 300 µm. The large melt pool width shows that the short scan lines create a large melt pool that moves along to the print direction. Using this scanning strategy, the FEM simulation can represent the thermal history better than using single track that causes tracks with varying track widths, allowing the coupling to microstructure CA model to be more accurate.

4.2.1.2 Simulated Grain Structure

The model first starts from the substrate having equiaxed grains approximately the size of 10 μm^3 and a single combined track is simulated (Figure 4-8). The grain structure shows competitive growth with grains having a more favourable orientation outgrowing the neighbouring grains forming larger grains as compared to the initial equiaxed grains. The favourable orientation of the

grains also differs at varying positions of the melt pool. From the top, the grains growing towards the centre and bending to the melt pool direction. In the centre, another grain blocks the grains from the side. The centre grains are formed from the bottom of the melt pool and grow vertically upwards which is seen in the cross section of the track. The grains that grew vertically grew faster than those from the side causing the centre grains seen from the top. The grains along the curvature of the melt pool grow towards the top-middle.

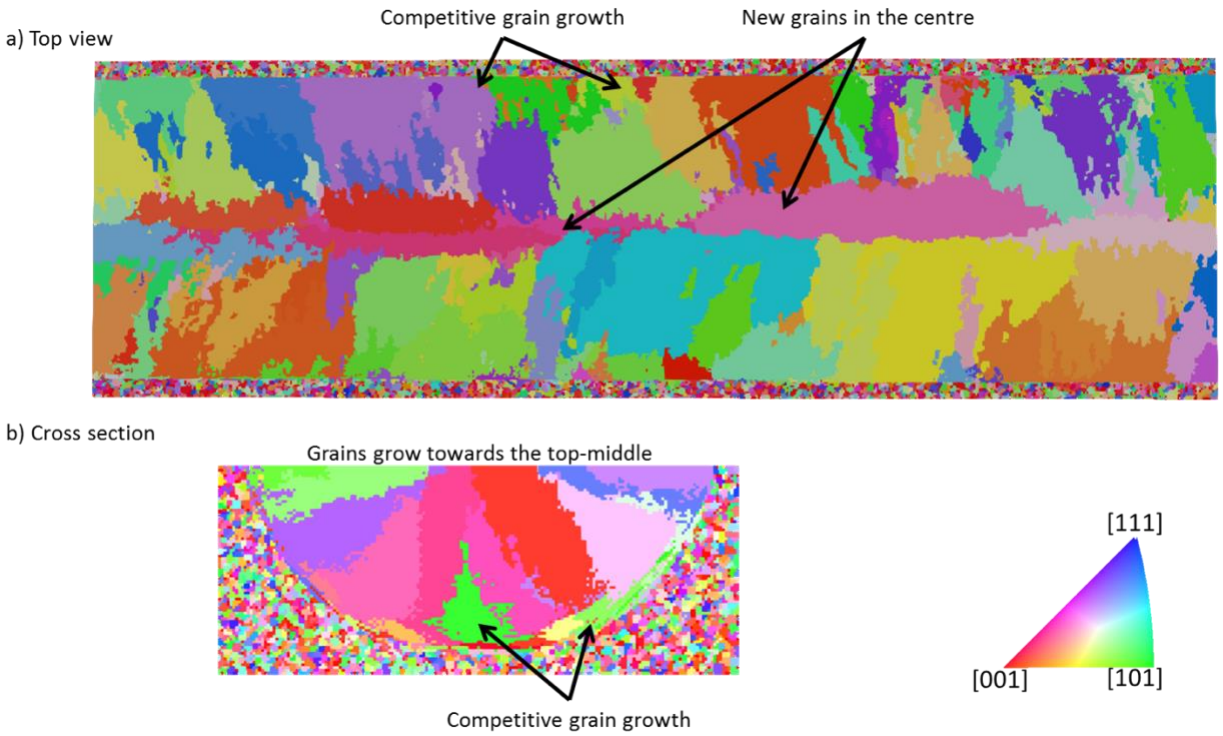

Figure 4-8 Simulated grain structure of a single combined track, viewed from a) top view, b) cross section. IPF-maps shown have the crystallographic orientations relative to the building direction.

To compare with experimental data, more tracks and layers have to be simulated. Three combined tracks were simulated per layer for two layers and the tracks were rotated 90° at the second layer as per experiment (Figure 3-7). As the simulated data is in 3D, it can give insights to the formation of the grain structure and 2D cross sections can be compared with experimental data. Figure 4-9 shows the grain structure simulated by the CA model. Unlike in a single track where grains grow

from the substrate, multiple tracks overlap each other causing grains to grow from previously melted tracks or layers. Due to the large difference in melt depth and powder layer thickness, only the bottom grains would remain and experience epitaxial growth. Although the top portion of the grains may have some variation from the bottom grains as seen in the single track, the grains would be remelted and lose the variations. Moreover, the combined tracks overlap each other causing the growth from the side to originate from a previously formed track. These lead to different patterns compared to the single track. The patterns seen in experimental data like grains going straight up and zigzag through the layers (Figure 4-6) are exhibited in the simulated grains as well (Figure 4-9). In the second layer, grain competition led to even coarser grains leading to variation of grain width within a layer. The bottom of the layer tends to have grain widths of approximately 100 to 400 μm while the top of the layer the grains becomes coarser getting as large as 1200 μm. However, majority of the top portion would be melted in the next layer and epitaxial growth would start from the bottom of the layer. This is likely the reason why the experimental data show grain widths of 100 to 600 μm in length. Both experimental data and simulated data have similar gain widths, however, more layers have to be simulated in order to get a clearer picture. As the layer thickness is only 50 μm, in order to get a large enough height, the simulation have to run for multiple layers and can take months.

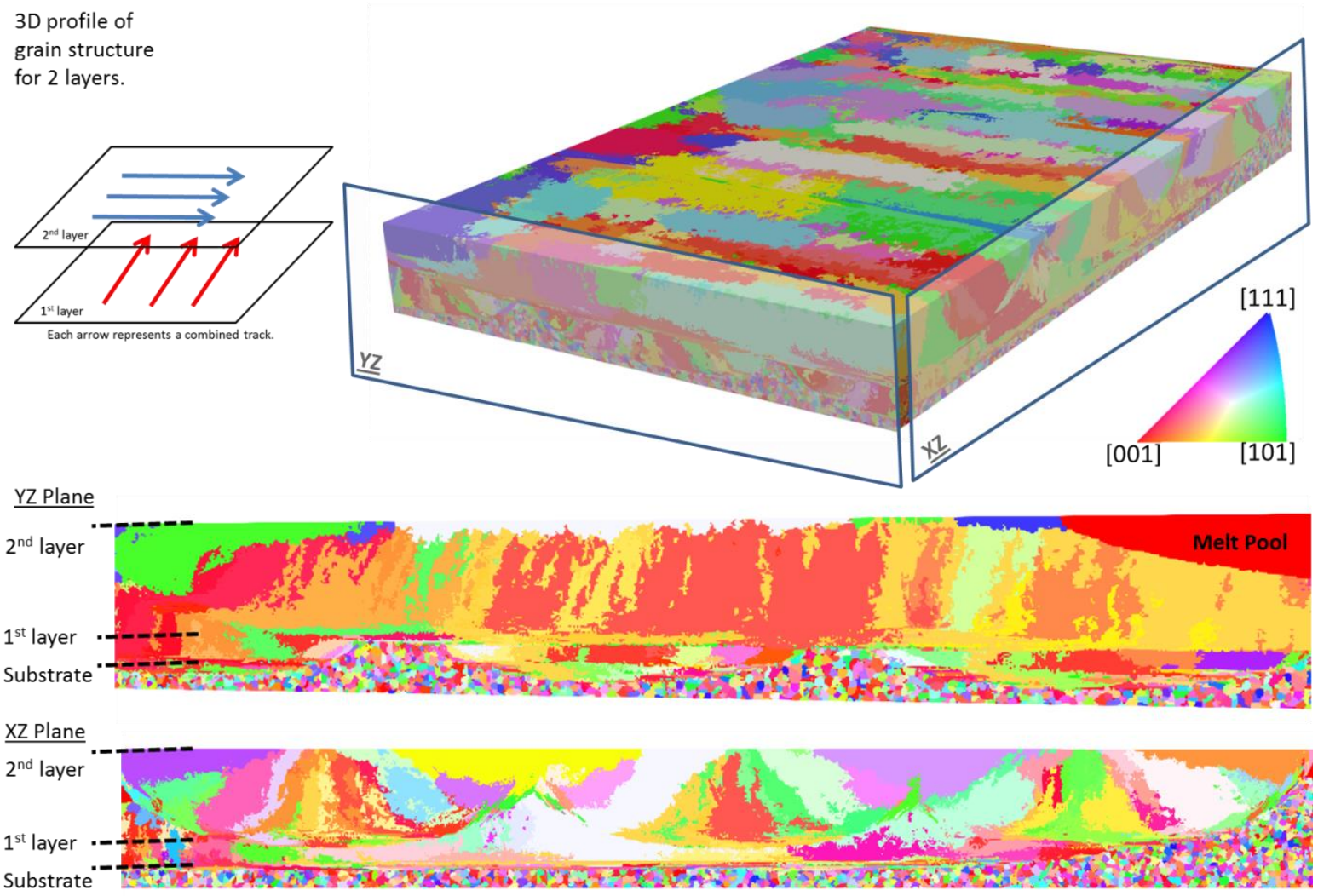

Figure 4-9 Top: Simulated grain structure in 3D with 3 combined tracks per layer for 2 layers, bottom: cross section of two planes showing the grain orientations. IPF-maps shown have the crystallographic orientations relative to the building direction.

4.2.2 Ti34Nb

The thermal and microstructure model can simulate different materials as long as the material is a metal with a cubic structure having <100> preferential growth direction. The models were altered to simulate for Ti34Nb printed using SLM. The changes were in the material properties and laser profile used in the thermal and microstructure models. Two cases were simulated and the scanning strategy for both is the same a combined track of width 1 mm. Case 1 uses 950 W laser power, 1 m/s scanning speed and top-hat beam profile and case 2 uses 350 W laser power, 0.35 m/s scanning speed and Gaussian beam profile.

4.2.2.1 FEM Model

The combined track of both cases leads to different melt pool dimensions. Case 1 using higher power laser and fast scanning speed caused a large melt pool to combine with the next few subsequent scans that lead to the melt pool becoming a much larger and moving in the direction of the combined track. Case 2 using lower power laser did not had as big a melt pool and the slower scanning speed lead to the melt pool cooling and solidifying before the next subsequent scan. Figure 4-10 shows the difference in melt pool geometry. The experimental result show an approximated melt pool width to average around 1000 μm and 200 μm for case 1 and 2 respectively [108]. In comparison, the FEM simulation found the melt pool width to be 1070 μm and 170 μm for case 1 and 2 respectively. There is a 7-15% difference between simulation and experiment, with the simulation overestimating melt pool width in the high laser power case while underestimating the width in the lower power case. A possible reason for this is that in the simulation, it was assumed that the material is already a Ti34Nb alloy while in the experiment, the powder bed was a mix of titanium and niobium powders and alloyed *in-situ*.

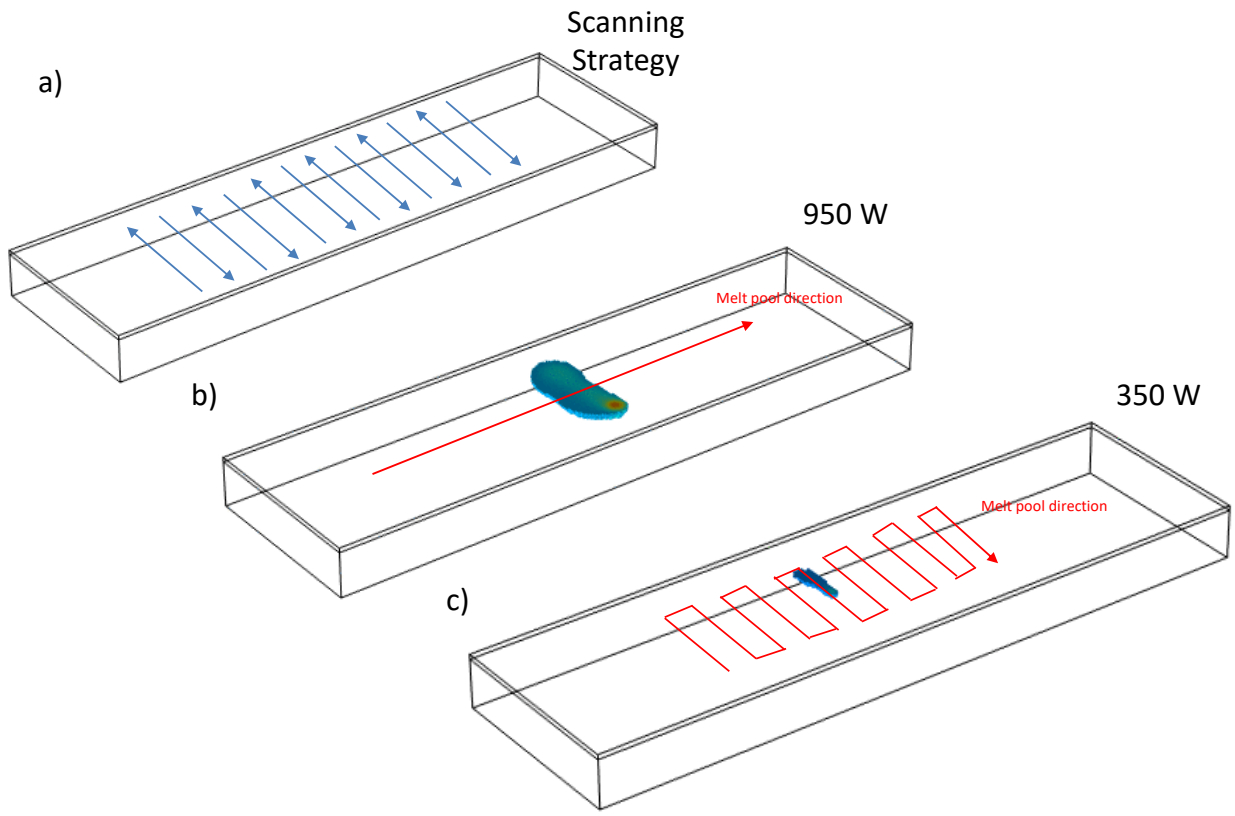

Figure 4-10 a) shows the scanning strategy applied to the FEM model, b) shows the melt pool shape and moving direction for high laser power and c) shows the melt pool shape and direction for low laser power.

4.2.2.1 Cellular Automata Model

The difference in melt pool sizes can lead to different grain sizes and was observed in the EBSD data where the average grain width of case 1 is 243 μm and case 2 is 71 μm [108]. The CA model found the average grain width to be 133 μm and 81 μm for case 1 and 2 respectively. The distribution of grain width between the simulation and experiment for case 1 and 2 are shown in Figure 4-11and Figure 4-12 respectively. In case 1, the grains tend to have a higher occurrence between 85 μm to 155 μm and tapers off after. The simulated results taper off quickly having a maximum grain width of 300 μm while the experimental results show there are grains that are much larger although they occur at much lower frequency. In case 2, the grain width tend to occur more between 30 μm to 90 μm and slowly taper off between 90 μm to 170 μm. Overall the

simulation managed to capture the trend of the distribution of the grain widths found in experimental data.

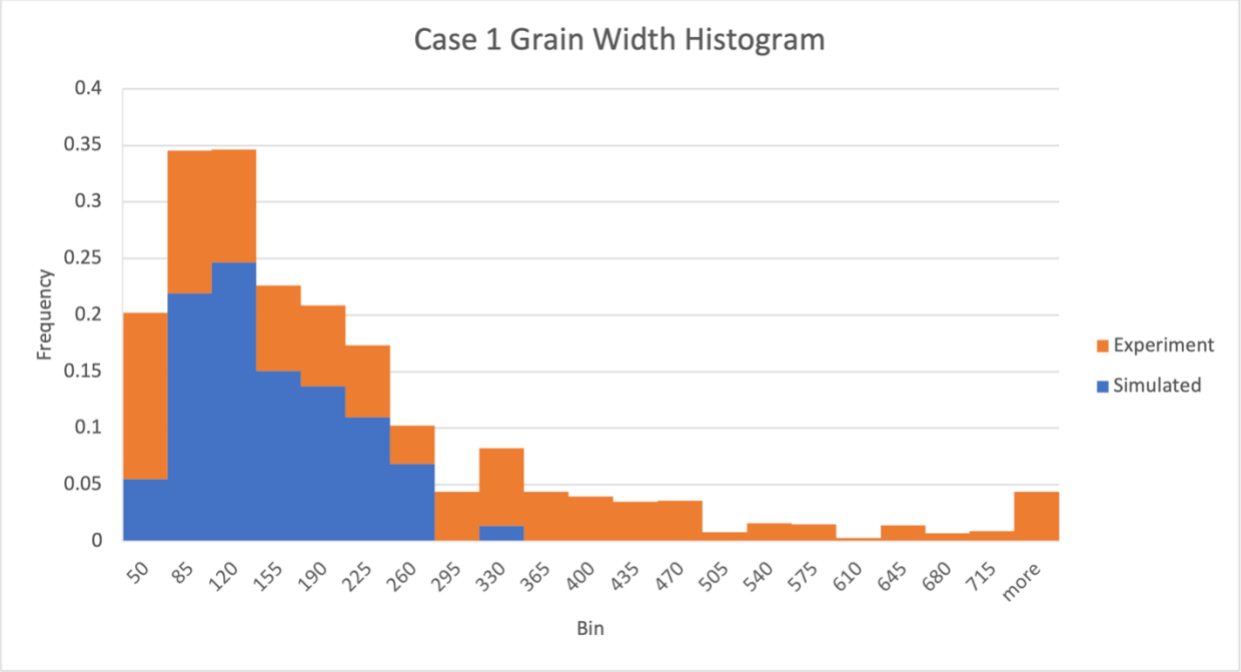

Figure 4-11 Grain width distribution of both simulation and experiment for case 1.

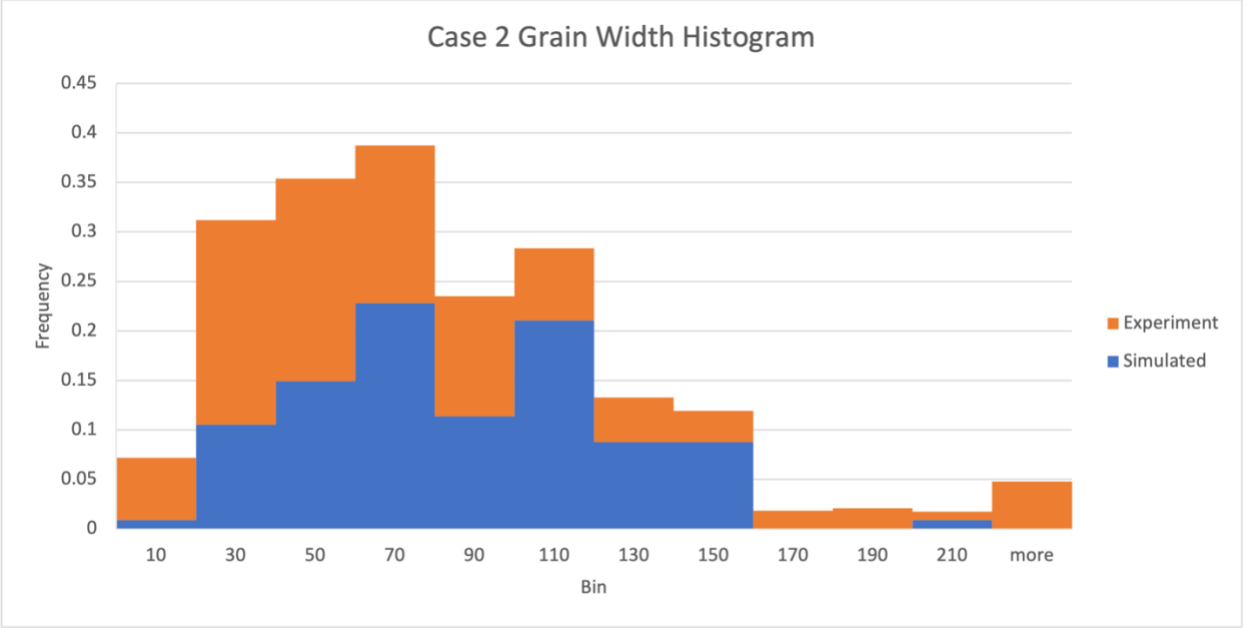

Figure 4-12 Grain width distribution of both simulation and experiment for case 2.

The difference in average grain width in case 1 might be due to the simulation only being in the first layer and the grains with <100> direction relative to build direction may need more than a few layers to competitively outgrow neighbouring grains. The simulated grains also show that in the first layer, there are still grains with other directions. The grain width in case 2 is quite close to the experiment, but there were not nucleated grains while the EBSD data showed multiple grains with random directions (Figure 4-13). These stray grains may be nucleated causing the stop to the growth of the <100> direction grains, thereby causing a smaller grain width.

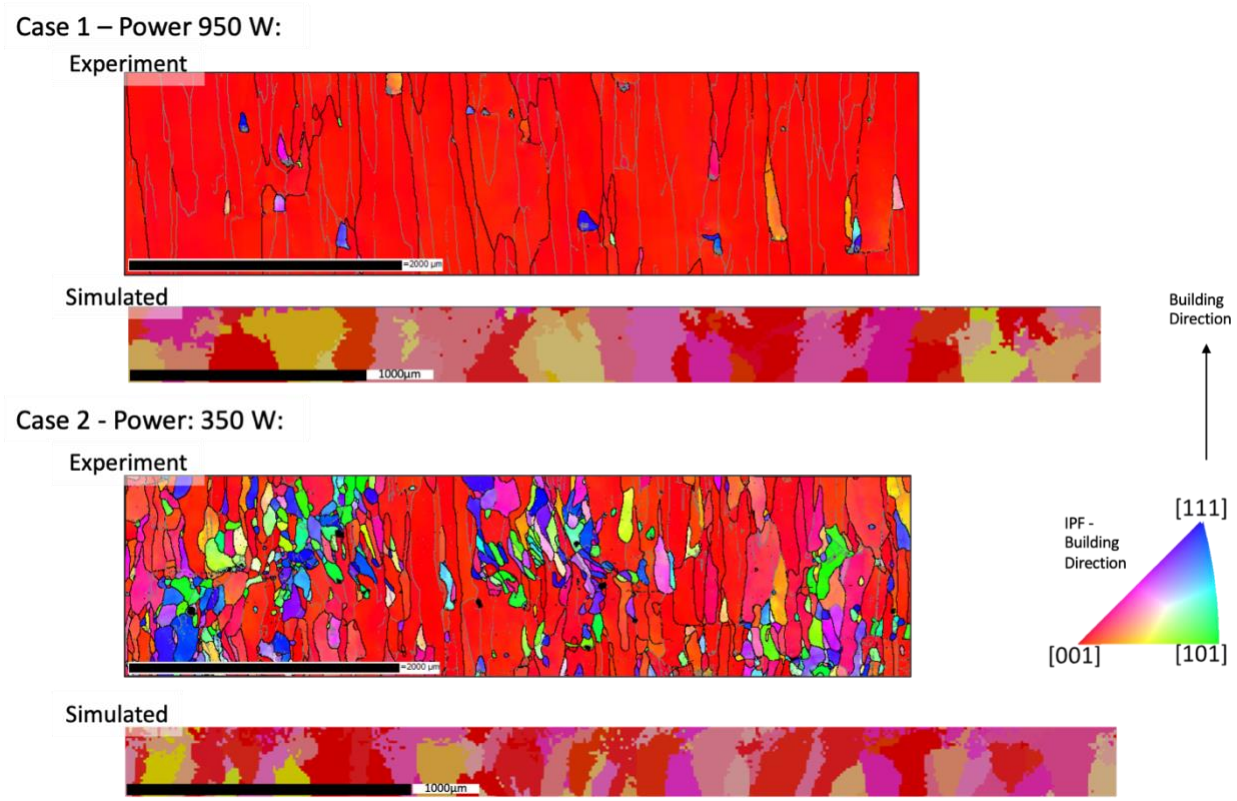

Figure 4-13 Comparison of EBSD and simulated results of printed Ti34Nb for both cases. The scale for the EBSD and simulated results are different. EBSD data is taken from Huang *et. al.* [108].

The EBSD results of case 1 showed that the majority of the grains are very close to the <100> direction relative to building direction. The height of the EBSD shows that the image was taken over a sample with more than hundreds of layers while the simulation was only for a single layer.

The simulation results didn't have all the grains at <100> direction and had the average grain width around 100 μm smaller, this may change if more layers are simulated and the <100> direction grains can out compete other grains increasing the size of the grain width as well as result in more grains <100> direction.

The CA model have implemented nucleation model used in casting simulation and found that moving melt pool does not fulfil the condition set by the nucleation model and would never nucleate. When the heat source is stopped at the end of the scan, the melt pool becomes stationery and cools towards the centre of the last heat source location. At that stage it becomes quite similar to solidification in casting, however, no nucleation occurred in the simulation of both cases. This may be because there is no study or literature providing the nucleation density and approximated undercooling temperature equiaxed grains form. However, it is more likely because the thermal gradient in the solidification area of the melt pool is very high which would not lead to formation of equiaxed grains [120]. EBSD images show stray grains with random crystal orientation appearing randomly with more appearing in case 2 than case 1. Huang *et. al.* suggest that this is due to un-melted niobium particles forming seeded sites for these stray grains to grow. This is not simulated in this CA model and may explain why stray grains are seen in the experiment data while not in the simulation.

4.3 Limitations and Challenges

The simulation models are not without limitations as certain assumptions must be in place in order to keep the model simple enough to run within a practical time frame. FEM models have a fixed geometry which is different from actual tracks, the mechanism behind the formation of the track geometry is not trivial and can have effects on the microstructure formation. The thermal gradient

affects solidification and is not the most accurate in FEM as convection in the melt pool is not simulated. An artificial increase in thermal conductivity was used but its effects would average out temperature in the melt pool rather than having higher cooling rates at certain areas where Marangoni effect is active. These effects affects how well the simulation can relate process parameters like the laser power and laser scanning speed, which would affect the melt pool depth and width. This is currently solved by tuning the laser absorptivity to align with experimental results, which is done in other literature as well [121, 122]. Going into further studies where optimizing process parameters is required, the model can then be affected when the parameters change significantly from the tuned parameters and would require running new experiments to further validate the simulated results. Both of these limitations can be addressed in CFD models, however, as mentioned in the literature review, simulating multiple tracks and layers using CFD may not be practical.

The CA model created for this study is limited to crystal structures that grow in the <100> direction. While most metals used in SLM currently fit into this limitation, study of new material that are not face centred cubic (FCC) or body cantered cubic (BCC) would not be possible with this model. Another assumption is that each cell assumes the growth would be mainly from the primary dendrite arms, but PFM models show it might be possible that the secondary dendrite arms grow faster in certain conditions [96]. This can affect the dendrite shape that is not simulated when using CA.

Challenges in the models include the need to simulate several layers to fully relate to the experiment data. In the SLM process, each layer thickness is often small, ranging from 30 to 80

μm and experimental data for grain structure like EBSD often are at least 1 mm in height. Simulating that would require approximately more than 20 layers, and each layer there may be multiple tracks required. CA model uses a much finer mesh and in this study was the bottleneck in simulation speed, using a different MATLAB license or coding it in C language and using Message Passing Interface (MPI) can allow the CA model to run using high performance computing which may help speed up the simulation.

Chapter 5 Conclusion & Future Works

5.1 Conclusion

In this research, the author created a CA model and showed the coupling of FEM and CA to simulate the thermal profile and resulting grain structure. Multiple tracks with varying scanning strategy, laser power and scanning speed were simulated and multiple layers were further simulated using CA. This shows that predicting the grain structure by simulation is possible and can help in reducing cost in experimenting. Two materials were simulated, stainless steel 316L and titanium-niobium alloy, with experimental validation of the grain structure created.

5.1.1 Cellular Automata Model

A CA model coded in MATLAB was shown to work in predicting grain structure with a given temperature profile. The CA model used dendrite growth theory to predict the growth of crystals given a certain undercooling temperature. Parallelization was explored for the CA model allowing the model to simualte in 3D in a reasonable time frame. For the current model, all 12 available workers can be used to run the code in parallel to achieve the fastest simulation speed.

5.1.2 Simulation and Experiment Data of stainless steel 316L manufactured using selective laser melting

For the simulation of SS 316L, a combined track which consists of multiple short single line tracks causes a large and slow-moving melt pool was used to print 10 × 10 × 5 mm cubes. The combined track was used as it provided more consistent tracks as compared to long single line track and this helps the simulation where FEM is used and the track geometry is fixed. In order to compare grain structure to experimental data, two layers were simulated with each layer containing three combined tracks. Results show similar patterns displayed in experimental data like zigzag grains across the layers, and grains fanning out as it grows between layers. Grain width varied at the bottom and top portion of the structure, with the bottom varying from 100 µm to 400 µm while the

top portion could grow much larger up to 1200 μm. However, the majority of the top portion would be remelted at the next layer causing epitaxial growth to start from the bottom portion which could lead to similar grain widths as seen in experimental data which range around 100 μm to 600 μm.

5.1.2 Simulation of titanium-niobium alloy manufactured using selective laser melting

For the simulation of Ti34Nb, two differing laser power and scanning speed were simulated. The results were compared against experimental result from a paper. Although the energy density was kept almost the same for both cases, the resultant melt pool geometry differed significantly. The high laser power and fast scanning speed lead to a large slow moving melt pool that moved perpendicular to the scanning direction while the low laser power and slower scanning speed lead to melt pool that move in accordance with the scanning strategy. This caused different grain structure, where the average grain width simulated was 133 μm and 81 μm for the high laser power and low laser power respectively. The EBSD data differed from the simulation for both cases, with the higher laser power differing by 100 μm, this may be because the simulation was only for one layer and more layers may be needed to see the competitive growth of the <100> crystallographic direction grains leading to larger widths. The lower laser power may also have cause un-melted niobium powders to act as nucleation sites impeding the growth of the grains causing the experimental data to have a smaller grain width than the simulated data.

5.1.3 Limitations of CAFE Simulation Model

Simulations shown in this research have several limitations. Assumptions are used in both FEM and CA models. The FEM model does not simulate the effects within the melt pool, which can lead to inaccuracies in the melt pool width and depth. This requires running experiments to validate and tune the model. This would also possibly cause inaccuracies in the cooling rate which can affect the growth rate of the grains when the temperature profile is added to the CA model.

However, using CFD may not be practical in simulating in a larger volume which is required for simulating different scanning strategies. The CA model used dendrite growth theory that limits it to metals that crystallographic structure grows in the <100>. This can limit the materials being able to simulated by the models presented. A challenge still remains the finer mesh of the CA model remains a bottleneck and would require more computing resources to be able to simulate faster. This is required when simulating for multiple layers.

5.2 Future Work

Manufacturing of metal parts using SLM provides a large amount of geometry freedom other conventional processes cannot do allowing highly customised shapes. In addition to that, SLM have the potential to create customised grain structure, if the process can create columnar or equiaxed grains *in-situ*.

Columnar and equiaxed microstructures would have varying anisotropy and mechanical properties [123]. The SLM process leads to steel, titanium alloys and Inconel alloys to form columnar, however with changes in process parameters, it is possible to change them to equiaxed grains [30, 124-127]. Equiaxed grains are formed when the dendrites in the melt pool grow towards a cooler point and the solute rejection from the dendrites causes a possibility of nucleation ahead of the dendrite growth. One of the ways to force equiaxed grains is by adding inoculating particles in the alloy which would become nucleuses that act as seeds to grow new grains [128]. This would change the material composition of the material.

Another way to achieve the columnar to equiaxed transition (CET) in an alloy is by getting the thermal gradient lower and solidification velocity higher. This is shown in Figure 5-1, for example

with SS 316L, if the thermal gradient is in the 10^4 K/m range, the solidification velocity has to be larger than $6x10^{-3}$ m/s in order to get equiaxed grains.

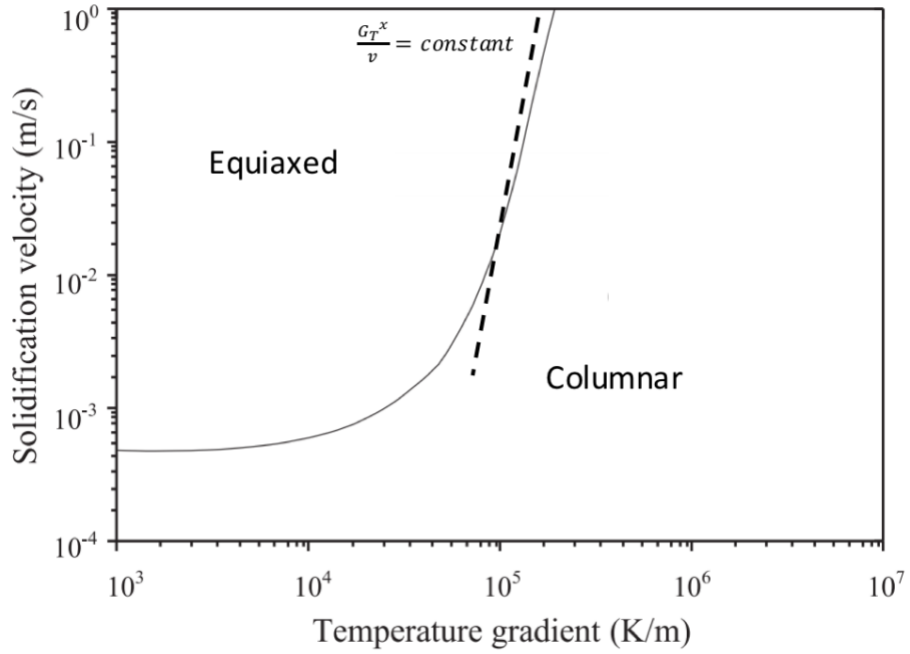

Figure 5-1 Columnar to equiaxed transition of SS 316 [129].

Changing the thermal gradient and solidification velocity is possible by changing laser parameters like laser scanning speed and duration, addition of a secondary laser source and laser [33, 53, 80, 130]. FEM simulation was carried out for SLM of SS316L to check the feasibility of achieving CET.

5.2.1 Columnar to Equiaxed Transition of Stainless Steel 316L

From the previous simulation of the combined track for SS 316L, a large melt pool was formed that moves slowly as compared to single track scans. In order to get more equiaxed grains, the grains have to be disrupted every layer to prevent columnar grains from growing through the layers.

Achieving lower thermal gradient would be essential in getting equiaxed grains as it can be almost impossible to get solidification speed high enough. To get lower thermal gradient, laser rescanning was explored. Two methods of laser rescanning were used, in both methods the scanning area and scanning strategy is the same, only difference is the laser power. In the first method, a lower laser power scans a small square and quickly followed by high laser power scanning the exact same square. The second method is the same except the high laser power scans first and low laser power seconds second. Both methods could reduce the temperature gradient of the melt pool in hope of achieving equiaxed grains.

One of the scanning strategies is the chessboard pattern which has squares with alternating horizontal and vertical stripe pattern as shown in Figure 5-2. FEM was carried out for a single square of size 500 x 500 µm. This was done as to produce one large melt pool that cools towards the centre in hope of forming equiaxed grains in the middle. The temperature gradient and growth velocity are calculated and sampled from the centre with a 300 µm radius and sampling interval of 50 µm. The data is then compared against the CET curve calculated for SS 316L. The output is then taken as the number of sampled data is above the CET curve. If more sampled points fall above the curve, the higher the chance of formation of equiaxed grains.

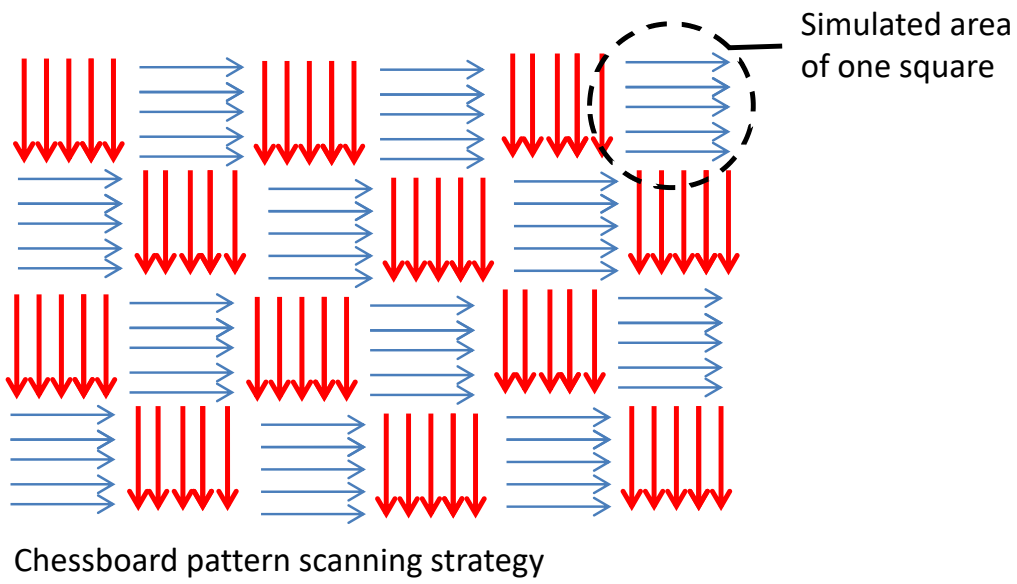

Figure 5-2 Illustration of the chessboard scanning strategy where each line is a single track scan.

Firstly, varying laser power and scanning speed were simulated and the hatch spacing was adjusted to keep the energy density constant at approximately 101 J/mm^3, as this was found to produce parts of low porosity [119]. It was found that laser power of 760 W and scanning speed of 3 m/s led to the largest number of points above the curve (Figure 5-3). These parameters would be used as the base for finding the rescanning parameters to be used.

Case	Laser Power (W)	Scanning Speed (m/s)	No. of points in equiaxed region
1	760	1.75	229
2	760	3.00	343
3	950	1.75	261
4	950	3.00	177

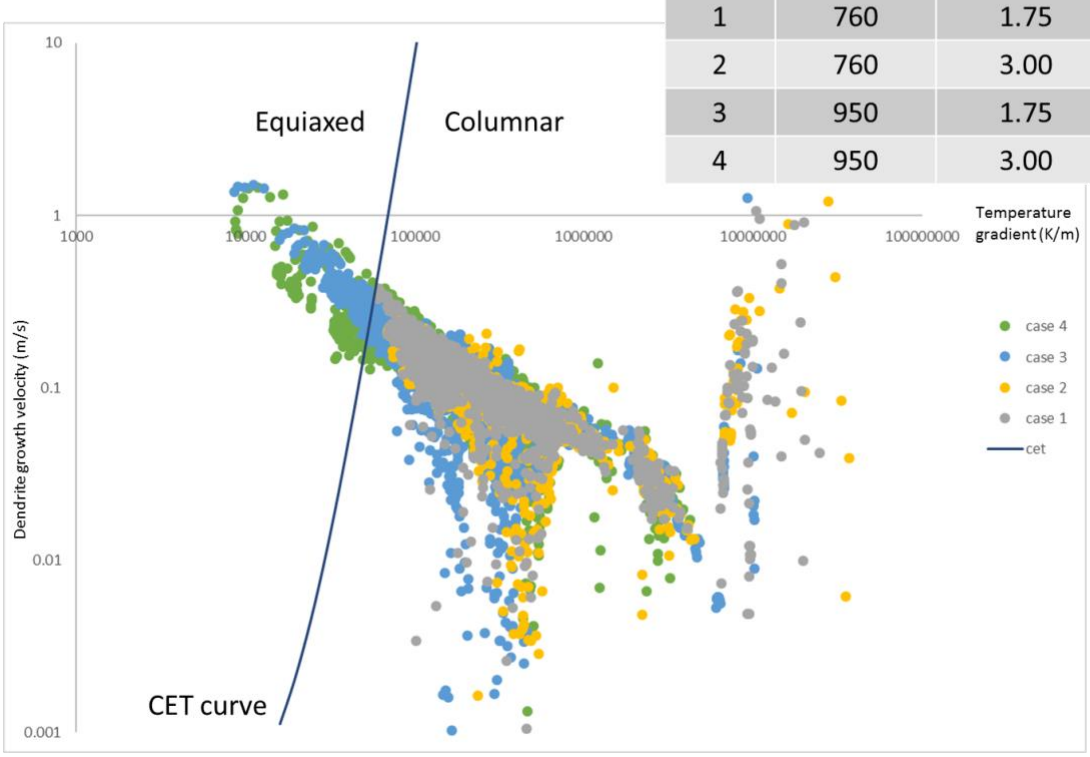

Figure 5-3 Sampled data points from four cases plotted with the CET curve.

To study the effects of rescanning, the FEM model did two laser scans. Both scans start from the same position and ends after scanning 500 µm in length. The scanning speed was kept constant in both the first and second scans and only varies the laser power. Cases 1 and 2 have the low power laser scan first followed by the high power laser. This led to some melting of powders and higher pre-heated temperatures. This caused the melt pool to have a lower temperature gradient during the solidification. Cases 3 and 4 have the higher power laser melting the powders first and before it solidifies, a low power laser rescans the area preventing the melt pool from cooling as quickly. This also caused a lower temperature gradient during solidification. Figure 5-4 shows the sampled data shifted left as compared to without rescanning. This causes more data points to fall in the equiaxed region showing that the rescanning can cause equiaxed grains in the centre of the scan.

Apart from case 3, all other cases show a decrease in temperature gradient and slight increase dendrite growth velocity and cases 2 and 4 have the largest increase in data points in the equiaxed range. Cases 2 and 4 both use the 760 W and 600 W laser power differing only in the sequence,

Case	Laser Power (W)	Scanning Speed (m/s)	Rescan Laser Power (W)	No. of points in equiaxed region
1	300	1.75	760	360
2	600	3.00	760	865
3	760	1.75	300	233
4	760	3.00	600	779

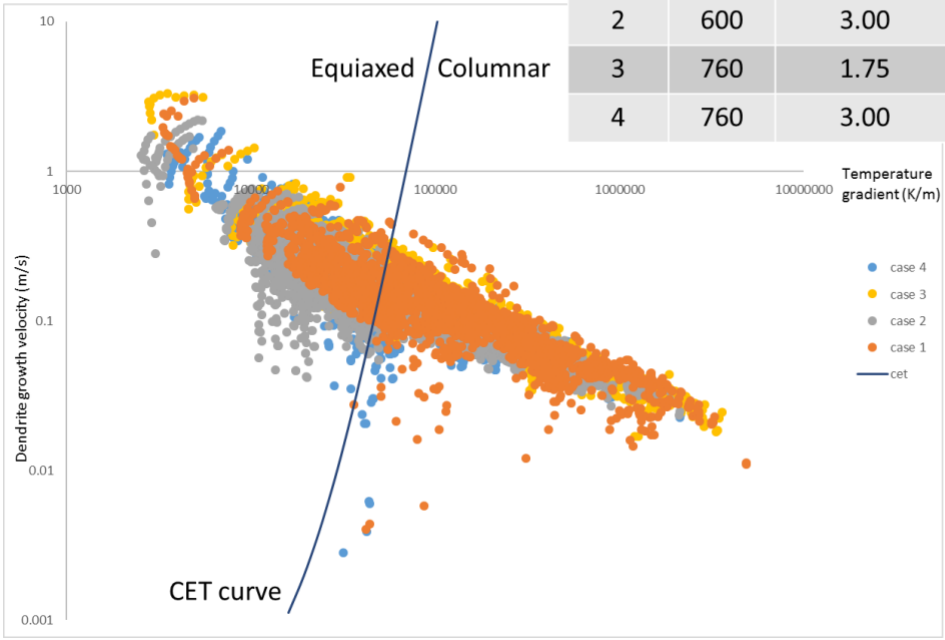

Figure 5-4 Sampled data of four laser rescanning cases plotted with the CET curve.

This preliminary study show that it may be possible to achieve CET in stainless steel manufactured using SLM. Laser rescanning can reduce the thermal gradient experience in certain portions of the melt pool during certain durations. More work must be done to ascertain this is true. Firstly, an FEM model is not the best model to use to determine thermal gradient in a melt pool, CFD models would make a better choice. No CA simulation was done for this, but the model is able to simulate if nucleation would occur, however, tuning may be required to determine the nucleation density. Experiment can be done to check if it works, but laser rescanning is not common in SLM machines and manually operation of the laser scanning may be required.

5.3 List of Publications

1. **Tan, J. H. K.**, Sing, S. L., & Yeong, W. Y. (2020) Microstructure modelling for metallic additive manufacturing: a review. *Virtual and Physical Prototyping, 15(1), 87-105*.
2. Huang, S., Narayan, R. L., **Tan, J. H. K.**, Sing, S. L., & Yeong, W. Y. (2021) Resolving the porosity-unmelted inclusion dilemma during in-situ alloying of Ti34Nb via laser powder bed fusion. *Acta Materialia*, *204*, 116522.

References

[1] E. Atzeni and A. Salmi, "Economics of additive manufacturing for end-usable metal parts," *Int. J. Adv. Manuf. Technol,* journal article vol. 62, no. 9, pp. 1147-1155, October 01 2012, doi: 10.1007/s00170-011-3878-1.

[2] I. Gibson, D. W. Rosen, and B. Stucker, *Additive manufacturing technologies*. Springer, 2010.

[3] D. M. Brunette, P. Tengvall, M. Textor, and P. Thomsen, *Titanium in medicine: material science, surface science, engineering, biological responses and medical applications*. Springer Science & Business Media, 2012.

[4] B. Cantor, H. Assender, and P. Grant, *Aerospace materials*. CRC Press, 2015.

[5] B. Vandenbroucke and J.-P. Kruth, "Selective laser melting of biocompatible metals for rapid manufacturing of medical parts," *Rapid Prototyping Journal,* vol. 13, no. 4, pp. 196-203, 2007.

[6] B. Baufeld, O. Van der Biest, and R. Gault, "Additive manufacturing of Ti-6Al-4V components by shaped metal deposition: Microstructure and mechanical properties," (in English), *Mater Design,* vol. 31, pp. S106-S111, Jun 2010, doi: 10.1016/j.matdes.2009.11.032.

[7] S. Vock, B. Klöden, A. Kirchner, T. Weißgärber, and B. Kieback, "Powders for powder bed fusion: a review," *Progress in Additive Manufacturing,* pp. 1-15, 2019.

[8] T. Christman, A. Needleman, S. Nutt, and S. Suresh, "On microstructural evolution and micromechanical modelling of deformation of a whisker-reinforced metal-matrix composite," *Mater. Sci. Eng., A,* vol. 107, pp. 49-61, 1989.

[9] M. Awd, J. Tenkamp, M. Hirtler, S. Siddique, M. Bambach, and F. Walther, "Comparison of microstructure and mechanical properties of Scalmalloy® produced by selective laser melting and laser metal deposition," *Materials,* vol. 11, no. 1, p. 17, 2018.

[10] D. Gu, W. Meiners, K. Wissenbach, and R. Poprawe, "Laser additive manufacturing of metallic components: materials, processes and mechanisms," *Int. Mater. Rev.,* vol. 57, no. 3, pp. 133-164, 2012.

[11] S. M. Yusuf and N. Gao, "Influence of energy density on metallurgy and properties in metal additive manufacturing," *Mater. Sci. Technol.,* vol. 33, no. 11, pp. 1269-1289, 2017/07/24 2017, doi: 10.1080/02670836.2017.1289444.

[12] S. Sakane, T. Takaki, M. Ohno, T. Shimokawabe, and T. Aoki, "GPU-accelerated 3D phase-field simulations of dendrite competitive growth during directional solidification of binary alloy," in *IOP Conference Series: Materials Science and Engineering*, 2015, vol. 84, no. 1: IOP Publishing, p. 012063.

[13] S. Chen, G. Guillemot, and C.-A. Gandin, "Three-dimensional cellular automaton-finite element modeling of solidification grain structures for arc-welding processes," *Acta Mater.,* vol. 115, pp. 448-467, 2016.

[14] J. A. Dantzig and M. Rappaz, *Solidification: -Revised & Expanded*. EPFL press, 2016.

[15] J. Lipton, M. Glicksman, and W. Kurz, "Dendritic growth into undercooled alloy metals," *Mater. Sci. Eng.,* vol. 65, no. 1, pp. 57-63, 1984.

[16] M. E. Glicksman, *Principles of solidification: an introduction to modern casting and crystal growth concepts*. Springer Science & Business Media, 2010.

[17] S. David and J. Vitek, "Correlation between solidification parameters and weld microstructures," *Int. Mater. Rev.,* vol. 34, no. 1, pp. 213-245, 1989.

[18] S. Kou, *Welding metallurgy*. John Wiley & Sons, 2003.

[19] M. C. Flemings, *Solidification processing*. Wiley Online Library, 1974.

[20] T. DebRoy and S. David, "Physical processes in fusion welding," *Rev. Mod. Phys.*, vol. 67, no. 1, p. 85, 1995.

[21] R. Trivedi and W. Kurz, "Dendritic growth," *Int. Mater. Rev.*, vol. 39, no. 2, pp. 49-74, 1994.

[22] G. Ivantsov, "Temperature around a spheroidal, cylindrical and acicular crystal growing in a supercooled melt," in *Dokl. Akad. Nauk*, 1947, vol. 58, pp. 567-569.

[23] J. Langer and H. Müller-Krumbhaar, "Theory of dendritic growth—I. Elements of a stability analysis," *Acta Metall.*, vol. 26, no. 11, pp. 1681-1687, 1978.

[24] R. Trivedi and W. Kurz, "Morphological stability of a planar interface under rapid solidification conditions," *Acta Metall.*, vol. 34, no. 8, pp. 1663-1670, 1986.

[25] J. Lipton, W. Kurz, and R. Trivedi, "Rapid dendrite growth in undercooled alloys," *Acta Metall.*, vol. 35, no. 4, pp. 957-964, 1987.

[26] W. Kurz, B. Giovanola, and R. Trivedi, "Theory of microstructural development during rapid solidification," *Acta Metall.*, vol. 34, no. 5, pp. 823-830, 1986.

[27] A. Basak and S. Das, "Epitaxy and microstructure evolution in metal additive manufacturing," *Annu. Rev. Mater. Res.*, vol. 46, pp. 125-149, 2016.

[28] R. C. Gifkins, "Grain-boundary sliding and its accommodation during creep and superplasticity," *Metall. Mater. Trans. A*, vol. 7, no. 8, pp. 1225-1232, 1976.

[29] L. E. Murr *et al.*, "Metal fabrication by additive manufacturing using laser and electron beam melting technologies," *J. Mater. Sci. Technol. (Shenyang, China)*, vol. 28, no. 1, pp. 1-14, 2012.

[30] T. T. Roehling *et al.*, "Modulating laser intensity profile ellipticity for microstructural control during metal additive manufacturing," *Acta Mater.*, vol. 128, pp. 197-206, 2017.

[31] W. E. Frazier, "Metal additive manufacturing: a review," *J. Mater. Eng. Perform.*, vol. 23, no. 6, pp. 1917-1928, 2014.

[32] J. J. Lewandowski and M. Seifi, "Metal additive manufacturing: a review of mechanical properties," *Annu. Rev. Mater. Res.*, vol. 46, pp. 151-186, 2016.

[33] N. Raghavan *et al.*, "Numerical modeling of heat-transfer and the influence of process parameters on tailoring the grain morphology of IN718 in electron beam additive manufacturing," *Acta Mater.*, vol. 112, pp. 303-314, 2016.

[34] R. Dehoff *et al.*, "Site specific control of crystallographic grain orientation through electron beam additive manufacturing," *Mater. Sci. Technol.*, vol. 31, no. 8, pp. 931-938, 2015.

[35] E. Atzeni and A. Salmi, "Economics of additive manufacturing for end-usable metal parts," *Int. J. Adv. Manuf. Technol*, vol. 62, no. 9-12, pp. 1147-1155, 2012.

[36] H. Piili, A. Happonen, T. Väistö, V. Venkataramanan, J. Partanen, and A. Salminen, "Cost estimation of laser additive manufacturing of stainless steel," *Phys. Procedia*, vol. 78, pp. 388-396, 2015.

[37] M. Baldinger, G. Levy, P. Schönsleben, and M. Wandfluh, "Additive manufacturing cost estimation for buy scenarios," *Rapid Prototyping Journal*, 2016.

[38] P. Mercelis and J.-P. Kruth, "Residual stresses in selective laser sintering and selective laser melting," *Rapid Prototyping Journal*, vol. 12, no. 5, pp. 254-265, 2006.

[39] K. Zeng, D. Pal, H. Gong, N. Patil, and B. Stucker, "Comparison of 3DSIM thermal modelling of selective laser melting using new dynamic meshing method to ANSYS," *Mater. Sci. Technol.*, vol. 31, no. 8, pp. 945-956, 2015.

[40] O. Zinovieva, A. Zinoviev, and V. Ploshikhin, "Three-dimensional modeling of the microstructure evolution during metal additive manufacturing," *Comput. Mater. Sci.,* vol. 141, pp. 207-220, 2018.

[41] L.-E. Loh *et al.*, "Numerical investigation and an effective modelling on the Selective Laser Melting (SLM) process with aluminium alloy 6061," *Int. J. Heat Mass Transfer,* vol. 80, pp. 288-300, 2015.

[42] M. Chiumenti *et al.*, "Numerical modelling and experimental validation in selective laser melting," *Addit. Manuf.,* vol. 18, pp. 171-185, 2017.

[43] A. Foroozmehr, M. Badrossamay, E. Foroozmehr, and S. Golabi, "Finite Element Simulation of Selective Laser Melting process considering Optical Penetration Depth of laser in powder bed," (in English), *Mater Design,* vol. 89, pp. 255-263, Jan 5 2016, doi: 10.1016/j.matdes.2015.10.002.

[44] V. Fallah, M. Alimardani, S. F. Corbin, and A. Khajepour, "Temporal development of melt-pool morphology and clad geometry in laser powder deposition," *Comput. Mater. Sci.,* vol. 50, no. 7, pp. 2124-2134, 2011.

[45] L.-E. Lindgren, H.-A. Häggblad, J. McDill, and A. S. Oddy, "Automatic remeshing for three-dimensional finite element simulation of welding," *Computer Methods in Applied Mechanics and Engineering,* vol. 147, no. 3-4, pp. 401-409, 1997.

[46] N. Patil *et al.*, "A Generalized Feed Forward Dynamic Adaptive Mesh Refinement and Derefinement Finite Element Framework for Metal Laser Sintering—Part I: Formulation and Algorithm Development," *Trans. ASME, Ser. B,* vol. 137, no. 4, p. 041001, 2015.

[47] E. R. Denlinger, "Development and Numerical Verification of a Dynamic Adaptive Mesh Coarsening Strategy for Simulating Laser Power Bed Fusion Processes," in *Thermo-Mechanical Modeling of Additive Manufacturing*: Elsevier, 2018, pp. 199-213.

[48] S. A. Khairallah, A. T. Anderson, A. Rubenchik, and W. E. King, "Laser powder-bed fusion additive manufacturing: Physics of complex melt flow and formation mechanisms of pores, spatter, and denudation zones," *Acta Mater.*, vol. 108, pp. 36-45, 2016.

[49] M. T. Andani, R. Dehghani, M. R. Karamooz-Ravari, R. Mirzaeifar, and J. Ni, "A Study on the Effect of Energy Input on Spatter Particles Creation during Selective Laser Melting Process," *Addit. Manuf.*, 2017.

[50] F. Gürtler, M. Karg, K. Leitz, and M. Schmidt, "Simulation of laser beam melting of steel powders using the three-dimensional volume of fluid method," *Phys. Procedia*, vol. 41, no. 1, pp. 874-879, 2013.

[51] P. Yuan and D. Gu, "Molten pool behaviour and its physical mechanism during selective laser melting of TiC/AlSi10Mg nanocomposites: simulation and experiments," *J. Phys. D: Appl. Phys.*, vol. 48, no. 3, p. 035303, 2015.

[52] C. Panwisawas *et al.*, "Mesoscale modelling of selective laser melting: Thermal fluid dynamics and microstructural evolution," *Comput. Mater. Sci.*, vol. 126, pp. 479-490, 2017.

[53] V. Fallah, M. Amoorezaei, N. Provatas, S. Corbin, and A. Khajepour, "Phase-field simulation of solidification morphology in laser powder deposition of Ti–Nb alloys," *Acta Mater.*, vol. 60, no. 4, pp. 1633-1646, 2012.

[54] Y. Lee and W. Zhang, "Mesoscopic simulation of heat transfer and fluid flow in laser powder bed additive manufacturing," in *International Solid Free Form Fabrication Symposium, Austin*, 2015, pp. 1154-1165.

[55] J. Zielinski, S. Vervoort, H.-W. Mindt, and M. Megahed, "Influence of powder bed characteristics on material quality in additive manufacturing," *Berg- Huettenmaenn. Monatsh.,* vol. 162, no. 5, pp. 192-198, 2017.

[56] Y. Lee and W. Zhang, "Mesoscopic simulation of heat transfer and fluid flow in laser powder bed additive manufacturing," in *Proceedings of the Annual International Solid Freeform Fabrication Symposium, Austin, TX, USA*, 2015, pp. 10-12.

[57] A. J. Pinkerton, "Advances in the modeling of laser direct metal deposition," *J. Laser Appl.,* vol. 27, no. S1, p. S15001, 2015.

[58] A. M. Rausch, V. E. Küng, C. Pobel, M. Markl, and C. Körner, "Predictive Simulation of Process Windows for Powder Bed Fusion Additive Manufacturing: Influence of the Powder Bulk Density," *Materials,* vol. 10, no. 10, p. 1117, 2017.

[59] D. Liu and Y. Wang, "Mesoscale Multi-Physics Simulation of Solidification in Selective Laser Melting Process Using a Phase Field and Thermal Lattice Boltzmann Model," in *ASME 2017 International Design Engineering Technical Conferences and Computers and Information in Engineering Conference*, 2017: American Society of Mechanical Engineers, pp. V001T02A027-V001T02A027.

[60] A. Rai, M. Markl, and C. Körner, "A coupled Cellular Automaton–Lattice Boltzmann model for grain structure simulation during additive manufacturing," *Comput. Mater. Sci.,* vol. 124, pp. 37-48, 2016.

[61] C. Körner, A. Bauereiß, and E. Attar, "Fundamental consolidation mechanisms during selective beam melting of powders," *Modell. Simul. Mater. Sci. Eng.,* vol. 21, no. 8, p. 085011, 2013.

[62] R. Degenhardt, "Advanced Lattice Boltzmann Models for the Simulation of Additive Manufacturing Processes," 2017.

[63] W. J. Seufzer, "Additive Manufacturing Modeling and Simulation A Literature Review for Electron Beam Free Form Fabrication," 2014.

[64] M. R. Rolchigo *et al.*, "Modeling of Ti-W solidification microstructures under additive manufacturing conditions," *Metall. Mater. Trans. A*, vol. 48, no. 7, pp. 3606-3622, 2017.

[65] C.-A. Gandin, J.-L. Desbiolles, M. Rappaz, and P. Thevoz, "A three-dimensional cellular automation-finite element model for the prediction of solidification grain structures," *Metall. Mater. Trans. A*, vol. 30, no. 12, pp. 3153-3165, 1999.

[66] T. M. Rodgers, J. D. Madison, and V. Tikare, "Simulation of metal additive manufacturing microstructures using kinetic Monte Carlo," *Comput. Mater. Sci.*, vol. 135, pp. 78-89, 2017.

[67] Z. Yang, S. Sista, J. Elmer, and T. DebRoy, "Three dimensional Monte Carlo simulation of grain growth during GTA welding of titanium," *Acta Mater.*, vol. 48, no. 20, pp. 4813-4825, 2000.

[68] D. Stefanescu, *Science and engineering of casting solidification*. Springer, 2015.

[69] F. Zhong, *Applications of Monte Carlo method in science and engineering*. InTech, 2011.

[70] Y. Liu *et al.*, "Monte Carlo simulation of polycrystalline microstructures and finite element stress analysis," *Mater Design*, vol. 55, pp. 740-746, 2014.

[71] S. Mishra and T. DebRoy, "Measurements and Monte Carlo simulation of grain growth in the heat-affected zone of Ti–6Al–4V welds," *Acta Mater.*, vol. 52, no. 5, pp. 1183-1192, 2004.

[72] S. Mishra and T. DebRoy, "Grain topology in Ti–6Al–4V welds—Monte Carlo simulation and experiments," *J. Phys. D: Appl. Phys.*, vol. 37, no. 15, p. 2191, 2004.

[73] H. Wei, J. Elmer, and T. DebRoy, "Three-dimensional modeling of grain structure evolution during welding of an aluminum alloy," *Acta Mater.*, vol. 126, pp. 413-425, 2017.

[74] T. M. Rodgers, J. D. Madison, V. Tikare, and M. C. Maguire, "Predicting mesoscale microstructural evolution in electron beam welding," *JOM,* vol. 68, no. 5, pp. 1419-1426, 2016.

[75] C.-A. Gandin and M. Rappaz, "A coupled finite element-cellular automaton model for the prediction of dendritic grain structures in solidification processes," *Acta Metall. Mater.*, vol. 42, no. 7, pp. 2233-2246, 1994.

[76] M. Rappaz and C.-A. Gandin, "Probabilistic modelling of microstructure formation in solidification processes," *Acta Metall. Mater.*, vol. 41, no. 2, pp. 345-360, 1993.

[77] H. Yin and S. Felicelli, "Dendrite growth simulation during solidification in the LENS process," *Acta Mater.*, vol. 58, no. 4, pp. 1455-1465, 2010.

[78] X. Zhan, Z. Dong, Y. Wei, and Y. Xu, "Dendritic grain growth simulation in weld molten pool based on CA-FD model," *Cryst. Res. Technol.,* vol. 43, no. 3, pp. 253-259, 2008.

[79] Z.-j. Wang, S. Luo, H.-w. Song, W.-d. Deng, and W.-y. Li, "Simulation of microstructure during laser rapid forming solidification based on cellular automaton," *Math. Probl. Eng.*, vol. 2014, 2014.

[80] A. R. A. Dezfoli, W.-S. Hwang, W.-C. Huang, and T.-W. Tsai, "Determination and controlling of grain structure of metals after laser incidence: Theoretical approach," *Sci. Rep.*, vol. 7, p. 41527, 2017.

[81] A. Zinoviev, O. Zinovieva, V. Ploshikhin, V. Romanova, and R. Balokhonov, "Evolution of grain structure during laser additive manufacturing. Simulation by a cellular automata method," *Mater Design,* vol. 106, pp. 321-329, 2016.

[82] O. Lopez-Botello, U. Martinez-Hernandez, J. Ramírez, C. Pinna, and K. Mumtaz, "Two-dimensional simulation of grain structure growth within selective laser melted AA-2024," *Mater Design,* vol. 113, pp. 369-376, 2017.

[83] I. Singer-Loginova and H. Singer, "The phase field technique for modeling multiphase materials," *Rep. Prog. Phys.,* vol. 71, no. 10, p. 106501, 2008.

[84] L. Gránásy, T. Pusztai, and J. A. Warren, "Modelling polycrystalline solidification using phase field theory," *J. Phys.: Condens. Matter,* vol. 16, no. 41, p. R1205, 2004.

[85] S. Sahoo and K. Chou, "Review on phase-field modeling of microstructure evolutions: application to electron beam additive manufacturing," in *ASME 2014 International manufacturing science and engineering conference, MSEC 2014 collocated with the JSME 2014 international conference on materials and processing and the 42nd North American manufacturing research conference*, 2014, pp. 9-13.

[86] M. M. Francois *et al.*, "Modeling of additive manufacturing processes for metals: Challenges and opportunities," *Curr. Opin. Solid State Mater. Sci.,* 2017.

[87] S. G. Kim and W. T. Kim, "Phase-Field Modeling of Solidification," *Handb. Mater. Model.,* pp. 2105-2116, 2005.

[88] W. J. Boettinger, J. A. Warren, C. Beckermann, and A. Karma, "Phase-field simulation of solidification," *Annu. Rev. Mater. Res.,* vol. 32, no. 1, pp. 163-194, 2002.

[89] I. Steinbach, "Phase-field models in materials science," *Modell. Simul. Mater. Sci. Eng.,* vol. 17, no. 7, p. 073001, 2009.

[90] L.-Q. Chen, "Phase-field models for microstructure evolution," *Annu. Rev. Mater. Res.,* vol. 32, no. 1, pp. 113-140, 2002.

[91] A. Farzadi, M. Do-Quang, S. Serajzadeh, A. Kokabi, and G. Amberg, "Phase-field simulation of weld solidification microstructure in an Al–Cu alloy," *Modell. Simul. Mater. Sci. Eng.*, vol. 16, no. 6, p. 065005, 2008.

[92] D. Montiel, L. Liu, L. Xiao, Y. Zhou, and N. Provatas, "Microstructure analysis of AZ31 magnesium alloy welds using phase-field models," *Acta Mater.*, vol. 60, no. 16, pp. 5925-5932, 2012.

[93] X. Gong and K. Chou, "Phase-field modeling of microstructure evolution in electron beam additive manufacturing," *JOM*, vol. 67, no. 5, pp. 1176-1182, 2015.

[94] T. Keller *et al.*, "Application of finite element, phase-field, and calphad-based methods to additive manufacturing of Ni-based superalloys," *Acta Mater.*, vol. 139, pp. 244-253, Oct 15 2017, doi: 10.1016/j.actamat.2017.05.003.

[95] S. Sahoo and K. Chou, "Phase-field simulation of microstructure evolution of Ti–6Al–4V in electron beam additive manufacturing process," *Addit. Manuf.*, vol. 9, pp. 14-24, 2016.

[96] R. Acharya, J. A. Sharon, and A. Staroselsky, "Prediction of microstructure in laser powder bed fusion process," *Acta Mater.*, vol. 124, pp. 360-371, 2017.

[97] C. Beckermann, H.-J. Diepers, I. Steinbach, A. Karma, and X. Tong, "Modeling melt convection in phase-field simulations of solidification," *J. Comput. Phys.*, vol. 154, no. 2, pp. 468-496, 1999.

[98] R. Wang, Y. Liu, and D. Q. Wei, "Microstructures in solidification simulation of electron beam scanning with MC in molten pool," in *Advanced Materials Research*, 2014, vol. 898: Trans Tech Publ, pp. 168-172.

[99] X. Zhou, H. Zhang, G. Wang, X. Bai, Y. Fu, and J. Zhao, "Simulation of microstructure evolution during hybrid deposition and micro-rolling process," *J. Mater. Sci.,* vol. 51, no. 14, pp. 6735-6749, 2016.

[100] M. A. Zaeem, H. Yin, and S. D. Felicelli, "Modeling dendritic solidification of Al–3% Cu using cellular automaton and phase-field methods," *Applied Mathematical Modelling,* vol. 37, no. 5, pp. 3495-3503, 2013.

[101] Y. Cao and J. Choi, "Multiscale modeling of solidification during laser cladding process," *J. Laser Appl.,* vol. 18, no. 3, pp. 245-257, 2006.

[102] Y. Zhang and J. Zhang, "Modeling of solidification microstructure evolution in laser powder bed fusion fabricated 316L stainless steel using combined computational fluid dynamics and cellular automata," *Addit. Manuf.,* vol. 28, pp. 750-765, 2019.

[103] Q. Yang, P. Zhang, L. Cheng, Z. Min, M. Chyu, and A. C. To, "Finite element modeling and validation of thermomechanical behavior of Ti-6Al-4V in directed energy deposition additive manufacturing," *Addit. Manuf.,* vol. 12, pp. 169-177, 2016.

[104] A. Rai, H. Helmer, and C. Körner, "Simulation of grain structure evolution during powder bed based additive manufacturing," *Addit. Manuf.,* vol. 13, pp. 124-134, 2017.

[105] J. Akram, P. Chalavadi, D. Pal, and B. Stucker, "Understanding grain evolution in additive manufacturing through modeling," *Addit. Manuf.,* vol. 21, pp. 255-268, 2018.

[106] B. Wysocki, P. Maj, R. Sitek, J. Buhagiar, K. J. Kurzydłowski, and W. Święszkowski, "Laser and electron beam additive manufacturing methods of fabricating titanium bone implants," *Appl. Sci.,* vol. 7, no. 7, p. 657, 2017.

[107] P. Liu, Z. Wang, Y. Xiao, M. F. Horstemeyer, X. Cui, and L. Chen, "Insight into the mechanisms of columnar to equiaxed grain transition during metallic additive manufacturing," *Addit. Manuf.*, vol. 26, pp. 22-29, 2019.

[108] S. Huang, R. L. Narayan, J. H. K. Tan, S. L. Sing, and W. Y. Yeong, "Resolving the porosity-unmelted inclusion dilemma during in-situ alloying of Ti34Nb via laser powder bed fusion," *Acta Mater.*, vol. 204, p. 116522, 2021.

[109] S. Safdar, A. J. Pinkerton, L. Li, M. A. Sheikh, and P. J. Withers, "An anisotropic enhanced thermal conductivity approach for modelling laser melt pools for Ni-base super alloys," *Applied mathematical modelling*, vol. 37, no. 3, pp. 1187-1195, 2013.

[110] K. C. Mills, *Recommended values of thermophysical properties for selected commercial alloys*. Woodhead Publishing, 2002.

[111] W. King, A. Anderson, R. Ferencz, N. Hodge, C. Kamath, and S. Khairallah, "Overview of modelling and simulation of metal powder bed fusion process at Lawrence Livermore National Laboratory," *Mater. Sci. Technol.*, vol. 31, no. 8, pp. 957-968, 2015.

[112] X. Zhan, Y. Wei, and Z. Dong, "Cellular automaton simulation of grain growth with different orientation angles during solidification process," *J. Mater. Process. Technol.*, vol. 208, no. 1, pp. 1-8, 2008.

[113] X. Lin, Y. Li, M. Wang, L. Feng, J. Chen, and W. Huang, "Columnar to equiaxed transition during alloy solidification," *Sci. China, Ser. E: Technol. Sci.*, vol. 46, no. 5, pp. 475-489, 2003.

[114] J. Strößner, M. Terock, and U. Glatzel, "Mechanical and microstructural investigation of nickel-based superalloy IN718 manufactured by selective laser melting (SLM)," *Adv. Eng. Mater.*, vol. 17, no. 8, pp. 1099-1105, 2015.

[115] M. Fischer, D. Joguet, G. Robin, L. Peltier, and P. Laheurte, "In situ elaboration of a binary Ti–26Nb alloy by selective laser melting of elemental titanium and niobium mixed powders," *Materials Science and Engineering: C,* vol. 62, pp. 852-859, 2016.

[116] M. A. Groeber and M. A. Jackson, "DREAM. 3D: a digital representation environment for the analysis of microstructure in 3D," *Integrating materials and manufacturing innovation,* vol. 3, no. 1, pp. 56-72, 2014.

[117] I. Yadroitsev, A. Gusarov, I. Yadroitsava, and I. Smurov, "Single track formation in selective laser melting of metal powders," *J. Mater. Process. Technol.*, vol. 210, no. 12, pp. 1624-1631, 2010.

[118] M. Ma, Z. Wang, and X. Zeng, "A comparison on metallurgical behaviors of 316L stainless steel by selective laser melting and laser cladding deposition," *Mater. Sci. Eng., A,* vol. 685, pp. 265-273, 2017.

[119] Z. Sun, X. Tan, S. B. Tor, and W. Y. Yeong, "Selective laser melting of stainless steel 316L with low porosity and high build rates," *Mater Design,* vol. 104, pp. 197-204, 2016.

[120] W. Kurz, C. Bezencon, and M. Gäumann, "Columnar to equiaxed transition in solidification processing," *Sci. Technol. Adv. Mater.,* vol. 2, no. 1, pp. 185-191, 2001.

[121] J. Ye *et al.,* "Energy coupling mechanisms and scaling behavior associated with laser powder bed fusion additive manufacturing," *Adv. Eng. Mater.,* vol. 21, no. 7, p. 1900185, 2019.

[122] G. Vastola, G. Zhang, Q. Pei, and Y.-W. Zhang, "Controlling of residual stress in additive manufacturing of Ti6Al4V by finite element modeling," *Addit. Manuf.,* vol. 12, pp. 231-239, 2016.

[123] J. Fu *et al.*, "Microstructure and Mechanical Properties of Ti-6Al-4V Fabricated by Vertical Wire Feeding with Axisymmetric Multi-Laser Source," *Appl. Sci.,* vol. 7, no. 3, p. 227, 2017.

[124] J. Raplee *et al.*, "Thermographic Microstructure Monitoring in Electron Beam Additive Manufacturing," *Sci. Rep.,* vol. 7, p. 43554, 2017.

[125] T. Niendorf, S. Leuders, A. Riemer, H. A. Richard, T. Tröster, and D. Schwarze, "Highly anisotropic steel processed by selective laser melting," *Metall. Mater. Trans. B,* vol. 44, no. 4, pp. 794-796, 2013.

[126] T. Niendorf *et al.*, "Functionally graded alloys obtained by additive manufacturing," *Adv. Eng. Mater.,* vol. 16, no. 7, pp. 857-861, 2014.

[127] L. Thijs, K. Kempen, J.-P. Kruth, and J. Van Humbeeck, "Fine-structured aluminium products with controllable texture by selective laser melting of pre-alloyed AlSi10Mg powder," *Acta Mater.,* vol. 61, no. 5, pp. 1809-1819, 2013.

[128] A. L. Greer *et al.*, "Grain refinement of aluminium alloys by inoculation," *Adv. Eng. Mater.,* vol. 5, no. 1-2, pp. 81-91, 2003.

[129] K. Zhang, S. Wang, W. Liu, and X. Shang, "Characterization of stainless steel parts by laser metal deposition shaping," *Mater Design,* vol. 55, pp. 104-119, 2014.

[130] S. Mokadem, C. Bezençon, A. Hauert, A. Jacot, and W. Kurz, "Laser repair of superalloy single crystals with varying substrate orientations," *Metall. Mater. Trans,* vol. 38, no. 7, p. 1500, 2007.